

REPORT DOCUMENTATION PAGE			Form Approved OMB No. 0704-0188		
<p>Public reporting burden for this collection of information is estimated to average 1 hour per response, including the time for reviewing instructions, searching existing data sources, gathering and maintaining the data needed, and completing and reviewing this collection of information. Send comments regarding this burden estimate or any other aspect of this collection of information, including suggestions for reducing this burden to Department of Defense, Washington Headquarters Services, Directorate for Information Operations and Reports (0704-0188), 1215 Jefferson Davis Highway, Suite 1204, Arlington, VA 22202-4302. Respondents should be aware that notwithstanding any other provision of law, no person shall be subject to any penalty for failing to comply with a collection of information if it does not display a currently valid OMB control number. PLEASE DO NOT RETURN YOUR FORM TO THE ABOVE ADDRESS.</p>					
1. REPORT DATE (DD-MM-YYYY) 07 April 2015		2. REPORT TYPE Journal Article		3. DATES COVERED (From - To) 17 March 2015 – 07 April 2015	
4. TITLE AND SUBTITLE Coupling between Hydrodynamics, Acoustics, and Heat Release in a Self-Excited Unstable Combustor			5a. CONTRACT NUMBER		
			5b. GRANT NUMBER		
			5c. PROGRAM ELEMENT NUMBER		
6. AUTHOR(S) Harvazinski, M.; Huang, C.; Sankaran, V.; Feldman, T.; Anderson, W.; Merkle, C.; Talley, D.			5d. PROJECT NUMBER		
			5e. TASK NUMBER		
			5f. WORK UNIT NUMBER Q0A1		
7. PERFORMING ORGANIZATION NAME(S) AND ADDRESS(ES) Air Force Research Laboratory (AFMC) AFRL/RQRC 10 E. Saturn Blvd Edwards AFB, CA 93524-7680			8. PERFORMING ORGANIZATION REPORT NO.		
9. SPONSORING / MONITORING AGENCY NAME(S) AND ADDRESS(ES) Air Force Research Laboratory (AFMC) AFRL/RQR 5 Pollux Drive Edwards AFB, CA 93524-7048			10. SPONSOR/MONITOR'S ACRONYM(S)		
			11. SPONSOR/MONITOR'S REPORT NUMBER(S) AFRL-RQ-ED-JA-2015-107		
12. DISTRIBUTION / AVAILABILITY STATEMENT Approved for public release; distribution unlimited					
13. SUPPLEMENTARY NOTES Journal article published in the AIP Physics of Fluids; Vol. #27, Number 4; 7 April 2015. PA Case Number: #15199; Clearance Date: 4/15/2015 © 2015 AIP Publishing LLC The U.S. Government is joint author of the work and has the right to use, modify, reproduce, release, perform, display, or disclose the work.					
14. ABSTRACT The unsteady gas dynamic field in a closed combustor is determined by the nonlinear interactions between chamber acoustics, hydrodynamics, and turbulent combustion that can energize these modes. These interactions are studied in detail using hybrid RANS/large eddy simulations (RANS = Reynolds Averaged Navier-Stokes) of a non-premixed, high-pressure laboratory combustor that produces self-excited longitudinal instabilities. The main variable in the study is the relative acoustic length between the combustion chamber and the tube that injects oxidizer into the combustor. Assuming a half-wave (closed-closed) combustion chamber, the tube lengths approximately correspond to quarter-, 3/8-, and half-wave resonators that serve to vary the phasing between the acoustic modes in the tube and the combustion chamber. The simulation correctly predicts the relatively stable behavior measured with the shortest tube and the very unstable behavior measured with the intermediate tube. Unstable behavior is also predicted for the longest tube, a case for which bifurcated stability behavior was measured in the experiment. In the first (stable) configuration, fuel flows into the combustor uninterrupted, and heat release is spatially continuous with a flame that remains attached to the back step. In the second (unstable) configuration, a cyclic process is apparent comprising a disruption in the fuel flow, subsequent detachment of the flame from the back step, and accumulation of fuel in the recirculation zone that ignites upon arrival of a compression wave reflected from the downstream boundary of the combustion chamber. The third case (mixed stable/unstable) shares features with both of the other cases. The major difference between the two cases predicted to be unstable is that, in the intermediate length tube, a pressure wave reflection inside the tube pushes unburnt fuel behind the back step radially outward, leading to a post-coupled reignition mechanism, while in the case of the longest tube, the reignition is promoted by vortex convection and combustor-wall interaction. Other flow details indicated by the simulation include the relative phase between flow resonances in the tube and the combustor, increased mixing due to baroclinic torque, and the presence of an unsteady triple flame					
15. SUBJECT TERMS					
16. SECURITY CLASSIFICATION OF:			17. LIMITATION OF ABSTRACT	18. NUMBER OF PAGES	19a. NAME OF RESPONSIBLE PERSON
a. REPORT Unclassified	b. ABSTRACT Unclassified	c. THIS PAGE Unclassified	SAR	29	D. Talley
					19b. TELEPHONE NO (include area code) N/A

Coupling between hydrodynamics, acoustics, and heat release in a self-excited unstable combustor

Matthew E. Harvazinski, Cheng Huang, Venkateswaran Sankaran, Thomas W. Feldman, William E. Anderson, Charles L. Merkle, and Douglas G. Talley

Citation: *Physics of Fluids* **27**, 045102 (2015); doi: 10.1063/1.4916673

View online: <http://dx.doi.org/10.1063/1.4916673>

View Table of Contents: <http://scitation.aip.org/content/aip/journal/pof2/27/4?ver=pdfcov>

Published by the [AIP Publishing](#)

Articles you may be interested in

[Response analysis of a laminar premixed M-flame to flow perturbations using a linearized compressible Navier-Stokes solver](#)

Phys. Fluids **27**, 043602 (2015); 10.1063/1.4918672

[Ignition sequence of an annular multi-injector combustor](#)

Phys. Fluids **26**, 091106 (2014); 10.1063/1.4893452

[On the compressible Hart-McClure and Sellars mean flow motions](#)

Phys. Fluids **24**, 096101 (2012); 10.1063/1.4748349

[Interactions between turbulence and flames in premixed reacting flows](#)

Phys. Fluids **23**, 125111 (2011); 10.1063/1.3671736

[Numerical characterization of hydrothermal waves in a laterally heated shallow layer](#)

Phys. Fluids **16**, 3839 (2004); 10.1063/1.1776963

An advertisement for AIP APL Photonics. It features a bright orange and yellow background with a sunburst effect. On the left is a small image of the journal cover, which shows a blue and white abstract pattern. To the right of the cover is a yellow starburst graphic with the words 'OPEN ACCESS' in red. The main text reads 'Launching in 2016!' in a large, white, sans-serif font, followed by 'The future of applied photonics research is here' in a smaller, white, sans-serif font. At the bottom right is the AIP APL Photonics logo, with 'AIP' in a large, white, sans-serif font and 'APL Photonics' in a smaller, white, sans-serif font.

Coupling between hydrodynamics, acoustics, and heat release in a self-excited unstable combustor

Matthew E. Harvazinski,¹ Cheng Huang,² Venkateswaran Sankaran,¹ Thomas W. Feldman,² William E. Anderson,² Charles L. Merkle,² and Douglas G. Talley¹

¹*Air Force Research Laboratory, Edwards AFB, California 93524, USA*

²*Purdue University, West Lafayette, Indiana 47907, USA*

(Received 8 October 2014; accepted 13 March 2015; published online 7 April 2015)

The unsteady gas dynamic field in a closed combustor is determined by the nonlinear interactions between chamber acoustics, hydrodynamics, and turbulent combustion that can energize these modes. These interactions are studied in detail using hybrid RANS/large eddy simulations (RANS = Reynolds Averaged Navier-Stokes) of a non-premixed, high-pressure laboratory combustor that produces self-excited longitudinal instabilities. The main variable in the study is the relative acoustic length between the combustion chamber and the tube that injects oxidizer into the combustor. Assuming a half-wave (closed-closed) combustion chamber, the tube lengths approximately correspond to quarter-, 3/8-, and half-wave resonators that serve to vary the phasing between the acoustic modes in the tube and the combustion chamber. The simulation correctly predicts the relatively stable behavior measured with the shortest tube and the very unstable behavior measured with the intermediate tube. Unstable behavior is also predicted for the longest tube, a case for which bifurcated stability behavior was measured in the experiment. In the first (stable) configuration, fuel flows into the combustor uninterrupted, and heat release is spatially continuous with a flame that remains attached to the back step. In the second (unstable) configuration, a cyclic process is apparent comprising a disruption in the fuel flow, subsequent detachment of the flame from the back step, and accumulation of fuel in the recirculation zone that ignites upon arrival of a compression wave reflected from the downstream boundary of the combustion chamber. The third case (mixed stable/unstable) shares features with both of the other cases. The major difference between the two cases predicted to be unstable is that, in the intermediate length tube, a pressure wave reflection inside the tube pushes unburnt fuel behind the back step radially outward, leading to a post-coupled reignition mechanism, while in the case of the longest tube, the reignition is promoted by vortex convection and combustor-wall interaction. Other flow details indicated by the simulation include the relative phase between flow resonances in the tube and the combustor, increased mixing due to baroclinic torque, and the presence of an unsteady triple flame. © 2015 AIP Publishing LLC. [<http://dx.doi.org/10.1063/1.4916673>]

I. INTRODUCTION

Confined reacting flows are often susceptible to an unwanted coupling between the flow dynamics and the heat release that can give rise to significant pressure oscillations. While the acoustic modes of the enclosing volume nearly always play a role in these oscillations, the problem is most interesting because the sources of coupling can involve multiple additional fluid dynamic phenomena. In the simplest and best understood interaction, a feedback path becomes established whereby a pressure variation leads directly to a change in the heat release. In such cases, amplification results when this heat release is in phase with the pressure as first explained by Lord Rayleigh.¹ The resulting oscillations are closely tied to the acoustic modes of the chamber. Representative examples of this type

of instability include flow in Rijke tubes,² liquid rocket engines,^{3,4} gas-turbines,^{5,6} ramjets,^{7,8} and scramjets.^{9,10} Varying levels of instabilities can arise and are almost always unwanted because of the increased vibrations, increased local heat transfer, flashback, and the uncontrolled overpressures that can result.

Pressure and velocity oscillations are, however, not limited to reacting flows. Purely hydrodynamic oscillations can also occur in non-reacting flows when acoustic modes resonantly lock on to vortex generation mechanisms in shear layers. Unstable interactions between a shear flow and a solid boundary have been reported by Rockwell, for flow over a cavity,¹¹ and by Ho and Nossier, for a free jet impinging on a plate.¹² Schmitt *et al.* have also observed interaction between non-reacting flow and acoustics when external forcing is used to excite the flow from a jet to examine the mixing enhancement that can occur under acoustic excitation.¹³

Such hydrodynamic instabilities arising when pressure pulses reflecting from the downstream end of the flow domain lock on to an upstream vortex generation mechanism are often amplified in reacting flows. In such “vortex-driven” combustion instabilities, the mixing variations produced by large-scale fluid dynamic motions can result in periodic heat release as first suggested by Rogers and Marble who considered screech instabilities in afterburners.¹⁴ Smith and Zukoski similarly observed self-excited vortex-driven combustion instability in an open-ended combustor with a back step used as a flame holder simulating a ramjet combustor.¹⁵ The instabilities were attributed to the impact of vortices from the back step impinging on the wall leading to periodically enhanced heat release. Yu *et al.* considered multiple dump combustor geometries in which the downstream end was terminated by an unchoked contraction. They attributed the observed convective instabilities to a coupling between pressure waves arising from vortex impingement off the contraction and the vortex shedding mechanism.¹⁶ Poinot *et al.* tested a dump combustor which was open to the atmosphere.¹⁷ Both vortex-driven modes and purely acoustic modes were observed, depending upon experimental conditions. Schadow *et al.* tested a variety of reacting and non-reacting configurations, culminated by the acoustic response of a non-premixed diffusion flame anchored by a back step downstream of a supersonic converging-diverging inlet. Their results showed a clear correlation between jet hydrodynamic modes and the most intense combustion oscillations. The oscillations also induced periodic fluctuations in the shock system in the upstream C-D inlet.^{18,19} In all these vortex-driven instabilities, the unstable frequencies are dependent upon a combination of the vortex convection time and the acoustic propagation time and so do not directly correspond to acoustic modes of the geometry.

A similar type of fluid-mechanic/acoustic oscillation can arise in confined chambers terminated by a nozzle. Entropy fluctuations produced by variations in heat addition can induce pressure fluctuations as the entropy wave passes through the nozzle. The intensity of the pressure perturbations increases with convective velocity, becoming a maximum when the nozzle is choked as first noted by Marble and Candel.²⁰ Goh and Morgans used an analytical model to study the impact of entropy waves on instability in combustors²¹ while RANS-based computations by Zhu *et al.*,²² Yao *et al.*,²³ and Hochgreb *et al.*²⁴ have likewise indicated that entropy fluctuations can impact instability in laboratory combustors. Most recently, Motheau *et al.* have demonstrated bulk-mode, entropy-acoustic coupling in large eddy simulations (LESs) of a gas turbine combustor with a choked downstream exit.²⁵ Again, the acoustics of the chamber are important, but the period is determined by a combination of entropy convection times and acoustic propagation times.

Other fluid dynamic interactions such as baroclinic vortex generation and local variations in flame geometrical characteristics can also be a factor in self-excited instabilities. Garby *et al.*²⁶ noted the importance of local variations in the flame characteristics and the presence of a triple flame phenomena. In addition to Garby’s findings, baroclinic vortex generation and cyclic heat release can be fundamental aspects of the flow. Transverse density gradients produced by heat release can interact with longitudinal pressure gradients produced by acoustics to give rise to vortices that impact mixing and unsteady heat release, in turn leading to pressure amplification when conditions are right. In addition to these experimental configurations that produce self-excited oscillations, another series of experiments address self-excited instabilities by using external forcing to deduce the combustion response. Among these are the works of Schuller *et al.*²⁷ and Ducruix *et al.*²⁸ In summary, self-excited instabilities commonly involve a wide range of fluid dynamic

TABLE I. Comparison of self-excited instability experiments.

Reference	Combustor to duct length ratio	Upstream boundary	Downstream boundary
Smith and Zukoski ¹⁵	0.47	Subsonic	Open
Poinsot <i>et al.</i> ¹⁷	0.18	Subsonic	Open
Yu <i>et al.</i> ¹⁶	0.04–0.29	Subsonic	Subsonic throat
Schadow <i>et al.</i> ^{18,19}	0.40–0.81	Choked C-D	Choked throat
Present work	2.00–4.28	Choked plate	Choked throat

interactions resulting from a lock-on of periodic pressure (or velocity) perturbations with classical fluid mechanic phenomena.

The present paper complements earlier work on self-excited instabilities by extending the geometrical parameters to a different regime as noted in Table I. Like the previous experiments of Smith and Zukoski, Yu *et al.*, Schadow *et al.*, and Poinsot *et al.*, the present work deals with an inlet/combustor configuration, but the length ratio is inverted. In the works of Yu *et al.* and Poinsot *et al.*, the combustor to inlet duct length ratio was small enabling the heat release zone to be treated as a compact region. The combustor/duct length ratio in Smith and Zukoski was larger (0.5), but the actual combustion occurred in the shadow of the backward facing step and could again be approximated as a compact region. The combustor lengths in the experiments of Schadow *et al.* were also shorter than the inlet duct, although the compact heat release approximation was probably not appropriate. By contrast, the combustor length in the present experimental configuration is longer than the inlet duct so that distributed heat release must be considered. In addition, the present experiment uses choked flow at both ends of the test configuration so that the upstream and downstream boundary conditions are more well-defined. Thus, the feedback between the combustion and fluid mechanics is fully described by the physics inside the combustor. The different geometrical emphases stem from application considerations. The earlier works were stimulated by issues in ramjet combustors and augmentors, whereas the present is stimulated by an interest in rocket combustors. It is noted that gas turbine combustors provide yet a third generic geometrical configuration. A unique aspect of the current work is that the inlet duct length is varied to correspond to quarter-, 3/8-, and half-wave resonators, which serve to vary the phasing between the acoustics in the duct and combustor. This duct length variation leads to the triggering of self-excited modes of different limit cycle amplitudes ranging from stable to unstable behavior. The impacts of this key geometrical parameter on the fluid dynamics and combustion phenomena help to provide a better physical understanding of the underlying physics driving the unstable behavior. Modeling these effects is the key focus of this study.

A substantial amount of work to model the coupling between flow dynamics and combustion has been done at a variety of fidelity levels. A low fidelity approach to revealing mechanisms that relate the combustion and fluid mechanics is so-called wave equation theory. In wave equation theory, the governing equations are expanded in terms of a small parameter or parameters and cast in the form of a wave equation that has a large number of source terms which can be grouped according to the order of the expansion.⁴ Different source terms can then be interpreted as different contributing mechanisms. If only the first order linear terms are retained, for example, only mechanisms controlling the initial growth rate are included. Energy exchange between modes leading to limit cycle behavior cannot be predicted unless the mechanisms contained in the second order (at least) non-linear terms are included and so on.

A limitation of wave equation-based theory is the difficulty in modeling the burning rate. The same may be said for many of the other ways; combustion instability has been modeled by means of various simplifications and/or approximations of the governing equations.^{3,4} A common approach is to model the burning rate as a transfer function or “combustion response,” in which fluctuations in the burning rate are assumed to be functions of fluctuations in other quantities. In the sensitive time lag theory,^{3,29} for example, fluctuations in burning rate are assumed to be proportional to fluctuations in pressure with a time delay. The problem with such simple assumptions is that they fail to capture the true complexity of the burning rate. More generally, if all the driving and

damping mechanisms cannot be predicted with sufficient accuracy, it will not be possible to accurately predict whether acoustic wave amplification will occur, i.e., the onset (or not) of combustion instabilities.

An emerging approach which may capture the salient mechanisms with sufficient accuracy is LESs. Work by Boudier *et al.*, Staffelbach *et al.*, and Motheau *et al.* has used LES to model combustion instability; their work has focused primarily on applications related to premixed gas turbines where a dynamically thickened flame turbulent closure is used.^{25,30,31} The same approach has also been applied to non-premixed conditions.^{26,32} In the case of gas turbine simulations, the instability level is typically much smaller than the instability level observed in rocket applications. Menon and co-workers have also applied LES to study combustion instability. Their work has primarily used the linear eddy model (LEM) for the combustion closure and has not been well resolved.^{33–35}

In this paper, a hybrid RANS/LES approach is used to simulate a model rocket combustor and the stability behavior that is observed experimentally. The hybrid RANS/LES approach allows for the resolution of the wall region while also capturing the unsteady large scale structures. Specifically, three geometric cases that show different behaviors (pressure, oscillation, and amplitude) are interrogated to help identify the dominant behaviors present. The computational results are compared with the experiment and are systematically analyzed to elucidate the complex interactions between the pressure waves and combustion phenomena. The results suggest baroclinic vorticity is an important driver in some instances helping to generate premixed regions susceptible to rapid combustion. This rapid depletion in fuel leads to a fuel cutoff event which sets up a cyclic pattern of burning. When the cyclic pattern of burning is in sync with the acoustics, unstable wave growth leading to a limit cycle is observed. The relative timings of waves arriving at the dump plane from the inlet tube and from the chamber determine how the relevant physics interact and ultimately whether or not the configuration is stable or unstable.

The remainder of this paper is organized as follows. In Sec. II, following an experimental and modeling overview of the study configuration and the model used in the present paper, a comparison of the simulations and experimental results is described. Results from the simulations are then analyzed in Sec. III to identify instability mechanisms, and a cycle analysis is presented in Sec. IV. A summary of the results and concluding remarks are given in Sec. V.

II. COMPARISON OF COMPUTATIONS AND EXPERIMENTS

A. Experimental review

The data simulated here were produced in a single element laboratory combustor specifically designed to study longitudinal combustion instabilities (direction of the wave propagation is aligned with the injector axis). The single element injector is of the ox-centered coaxial type, where warm oxidizing gas (decomposed hydrogen peroxide) is introduced via a central oxidizer post (ox-post), and fuel is introduced through a co-annular region at the downstream end of the central post. Longitudinal instabilities can be spontaneously produced or suppressed by changing the length of ox-post and the length of the combustion chamber.

The experiment is one of a series of spontaneously unstable model combustors originated by Miller *et al.*³⁶ who studied the effects of different lengths of the combustion chamber by adding or removing sections. Different lengths were found to produce different amplitudes of longitudinal instability as well as different dominant modes. Following this work, Sisco³⁷ explored the effects of the length of the ox-post and its inlet type (sonic or sub-sonic entry). The basic idea of these studies lay in the observation that unstable modes can result when the post and the chamber are tuned to excite resonant modes. In other words, for the sonic-inlet post, designing the post and chamber to both behave as half-wave resonators would potentially lead to the constructive amplification of disturbances. Likewise, de-tuning the post and chamber configurations would cause the waves to cancel each other, potentially leading to stable operation. Sisco's experiments demonstrated these trends by observing stable and unstable behaviors as a function of the post length, although the half-wave post and chamber combination did not necessarily lead to the maximum instability amplitudes. Moreover, Sisco³⁷ also investigated the influence of the back-step height on

TABLE II. Operating conditions.

Parameter	Value
Fuel mass flow rate, kg/s	0.027
Fuel temperature, K	300
Oxidizer mass flow rate, kg/s	0.320
Oxidizer temperature, K	1030
Oxidizer percent, H ₂ O	57.6
Oxidizer percent, O ₂	42.4
Equivalence ratio, (F/O)/(F/O) _{stoic}	0.8
Mean pressure, MPa	1.3

the instability amplitudes, which suggested that, in addition to the acoustics, hydrodynamics also play an important role.

Yu *et al.*^{37,38} redesigned the experiment with computational fluid dynamics (CFD) validation in mind. The inlet was modified to admit oxidizer through a series of choked, circumferential slots to reduce upstream influences and simplify CFD mesh generation. The liquid fuel of earlier experiments was changed to gaseous methane to eliminate uncertainties associated with modeling atomization and two-phase combustion. Finally, an electromechanically actuated inlet was designed to continuously vary the ox-post length during a firing, and the rig was renamed as Continuously Variable Resonance Combustor (CVRC). The ox-post length at transition (stable-to-unstable and unstable-to-stable) could be determined more precisely, and both stable and unstable behaviors could be observed in a single firing. Feldman³⁹ added optical access to the CVRC for spatio-temporal observation of the combustion field. High-speed imagery of the CH* radical showed clear changes in the unsteady combustion field as pressure oscillation amplitude changed.

The CVRC experimental configurations simulated in this paper are those studied by Yu *et al.*^{37,38} as imaged by Feldman.³⁹ A summary of the operating conditions is shown in Table II. The corresponding mean chamber pressure is nominally 1.3 MPa. A diagram of the experiment is shown in Figure 1. The oxidizer, initially 90% hydrogen peroxide, was fed into the gas generator where it was catalyzed. The oxidizer then entered the manifold as decomposed hydrogen peroxide through four concentric choked slots. The choked condition in the injector isolates the manifold from the oxidizer post and combustor. The length of the oxidizer post was varied from 19.1 cm to 8.9 cm, with an accuracy of approximately ± 0.3 cm. The gaseous methane was injected through an annular slot just upstream of the back step. The combustor is 38.1 cm long and a choked converging diverging nozzle is affixed to the end of the combustor. The choked boundaries upstream eliminate the influence from the manifold and the choked nozzle downstream is purely transmitting, removing

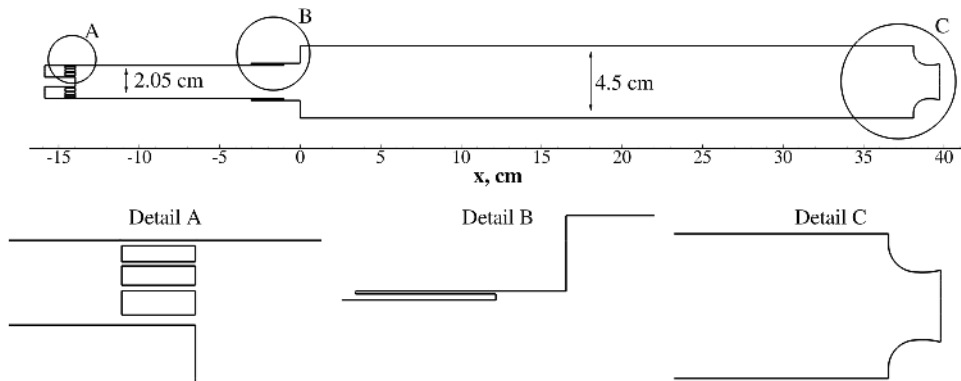


FIG. 1. Diagram of the CVRC experiment. Oxidizer enters from the choke slots (detail A) and fuel enters just upstream of the back step (detail B). A choked nozzle is affixed to the end of the combustor (detail C).

influence from the ambient conditions. These well-defined boundaries yield repeatable results, with the exception of bifurcated stability behavior at configurations with a long post. Whereas both stable and unstable operations were measured with this configuration; the simulation predicts only high-amplitude, unstable behavior.

B. Modeling review

Smith *et al.*⁴⁰ modeled the experiments of Sisco.³⁷ One important trend that Smith was able to reproduce was the effect of back step height on instability. The experiment and simulation were done to test the theory that instability was controlled by a synchronized mechanism comprising vortex shedding, vortex impingement on the combustor wall, and reinforcement of an upstream-running compression wave by the sudden increase of heat that occurred when the vortex hits the wall. Simulations showed that vortex impingement occurred closer to the back step for the small step height and promoted instability at higher frequencies. For a larger step height, the impingement occurred further downstream and the vortex partially decayed before impingement. The timing of this event was not well correlated with the acoustic mode. Smith *et al.*^{41,42} also performed companion simulations of the CVRC in two-dimensions showing that some general trends could be captured but the harmonic nature of the higher modes was not realized. Higher modes tended to be broad and not well defined unlike the experimental results, which had distinct peaks. Simulations also predicted unstable behavior for all oxidizer post lengths, while experiments showed stable combustion for the extremely short and long lengths. Three-dimensional simulations of these data by Harvazinski *et al.*^{43,44} for the unstable configurations showed that the simulations were able to produce larger amplitude pressure oscillations compared to the axisymmetric simulations and capture the higher order harmonics showing strong, well-defined peaks similar to the experiment. Feldman *et al.*⁴⁵ modeled experiments in three dimensions and provided a detailed comparison of the unstable experiment and the simulation. Although the simulation predicted overall lower levels of instability, many features were well captured by the simulation including the steepened wave fronts, rate of pressure rise, and mode shape.

The subject experiments were conducted in an uncooled, heat-sink chamber using short run times to prevent wall damage. Anecdotal evidence suggested that the instabilities tended to become stronger as the heat loss to the walls decreased. Computations with and without heat flux by both Smith⁴¹ and Garby *et al.*⁴⁶ are in qualitative agreement with this observation. Smith,⁴¹ using a heat loss of approximately 12%, found a small reduction in the instability amplitude, while Garby *et al.*,⁴⁶ using heat losses of nearly 40%, found that heat loss damped the instability while an adiabatic wall computation was unstable. Smith's heat loss assumptions were chosen upon the basis of heat loss measurements in a generically similar experiment by Pal *et al.*,⁴⁷ whereas Garby *et al.*⁴⁶ estimated the heat losses by the difference between the theoretical and measured chamber pressures in the present experiment. Accordingly, heat loss represents a potentially important parameter because of its ability to change the combustor temperature and thus the dominant frequency.

Garby *et al.*²⁶ also used the present experiment with a post length of 12.0 cm to assess the predictive capability of two-dimensional simulations and found similar results to those of Harvazinski *et al.*,⁴⁴ namely, that two-dimensional simulations were predictive of some phenomena but lacked the ability to capture the amplitude of the instability. The existence of a triple flame structure in the combustor was also suggested as a key element in the instability mechanism. It is noted that these previously reported simulations of the CVRC device have considered only the middle of the highly unstable region.

Srinivasan *et al.*³⁵ modeled the CVRC at three distinct oxidizer post lengths, 9.0 cm, 12.0 cm, and 14.0 cm. The LESs were three-dimensional and used the LEM sub-grid closure for turbulent chemistry interaction. A two-step global reaction was used to model the kinetics. They found that frequencies were over predicted by approximately 15%. Amplitudes for stable condition (short oxidizer post length) were higher than the experiment, over predicted by a factor of 4. Simulations of the two unstable lengths underpredicted the amplitudes by a factor of 2. Their simulation showed highly oscillatory flames in the combustor and peak heat releases inside the cup region for all three oxidizer post lengths.

To the authors' knowledge, no work describing all three regimes of the CVRC has been published. The present results include not only this highly unstable regime at an ox-post length of 14.0 cm but also the moderately stable regimes at ox-post lengths of 8.9 cm and 19.1 cm in an attempt to elucidate the physical mechanisms leading to this change in behavior. As noted later, our results for the mid-post length of 14.0 cm are very similar to the 12.0 cm post-length calculations of Garby *et al.*^{26,46}

C. Computational approach

The present simulations are based on numerical solutions of the Navier-Stokes, energy, and species equations.^{48–51} The numerical scheme is second-order accurate in both time and space and uses an implicit formulation allowing for the use of high-aspect ratio grids near the wall. A dual-time formulation is used to eliminate approximate factorization errors. Turbulence is modeled using a hybrid RANS/LES formulation,^{52,53} where the near wall is modeled using a two-equation k - ω model.^{54,55} Hybrid RANS/LES allows for a significant reduction in the number of grid points for wall bounded flows compared to a wall resolved LES and has advantages over wall-law LES in problems like the present where separation plays a dominant role. In the hybrid model, the calculated turbulent length scale from the k - ω model is compared to the local grid size. If the local grid size is smaller, the turbulent length scale in the transport equation for k is replaced with the local grid size. This has the effect of directly capturing the large scale unsteadiness in the flow and reducing the amount of turbulent kinetic energy that is modeled.

Combustion is accounted for using a single step global reaction⁵⁶ with laminar kinetics. Global reactions allow for the coupling between pressure and heat release while also minimizing the number of species that must be retained. No turbulent combustion closure is included; nearly, all closures are based on a constant pressure which brings into question the pressure response needed. An exception is the thickened flame model, which is not primarily intended for non-premixed combustion.⁵⁷ Our preliminary assessment suggests that the thickened flame model has little influence on the present calculations. A time step of 0.1 μ s is used, and simulations are run for 40 ms to provide sufficient cycles for analysis. All computations are three-dimensional and contain approximately 5×10^6 grid points. A study on the effect of grid size was completed for the 14.0 cm oxidizer post length using a combination of two- and three-dimensional simulations; results showed that the three-dimensional results compared well with a fine grid two-dimensional result.⁴⁴ Complete details of the simulation procedure can be found in Ref. 44.

D. Power spectral density (PSD) characteristics

The oscillatory pressure-time history of a single experiment in which the length of the oxidizer post was decreased from 19.1 to 8.9 cm is shown in Figure 2. A line showing the oxidizer post length as a function of time is superimposed. Although Figure 2 shows significant pressure variation at the beginning of the test, bandpass filtering the pressure signal at a frequency corresponding to the 1L mode indicates that combustion is relatively stable and peak-to-peak pressure oscillations at that frequency are about 160 kPa (about 12% of the mean). When the post length reaches 18 cm, the oscillations jump in magnitude to over 400 kPa (about 30% of the mean). Between 14 cm and 12 cm, the amplitude of the bandpass-filtered signal around the 1L mode frequency is about 400 kPa. The pressure oscillations decay slowly with further reductions in post length, and by 9 cm, the amplitude of the 1L mode oscillation is about 120 kPa (less than 10% of the mean). Henceforth, these regimes will be referred to as stable (post length greater than 18 cm), unstable (post length between about 18 and 10 cm), and moderately stable (post length less than 10 cm).

Figure 2 shows the variation in the amplitude of the peak PSD of the first mode as a function of oxidizer post length for multiple experiments including repeated runs at the same conditions, short to long post-length traverses to contrast with long to short traverses, and fixed post-length tests. As can be seen, the global results were quite consistent with a peak at mid-lengths and lower oscillations at the two extremes. This behavior suggests that different mechanisms of instability are

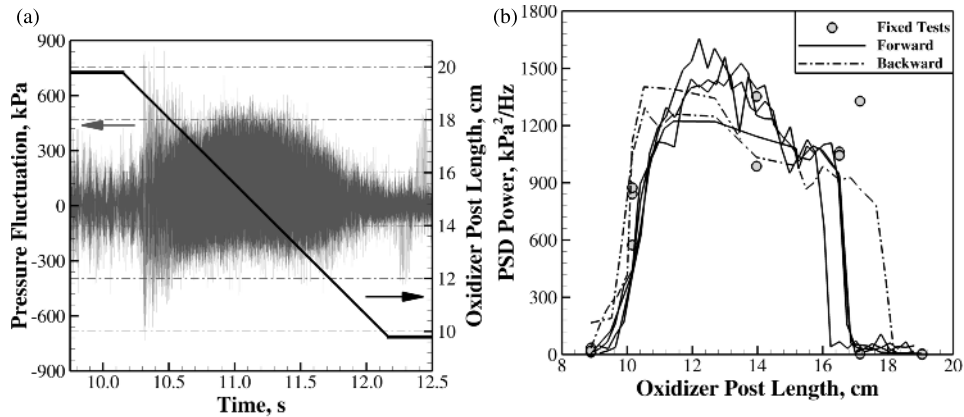


FIG. 2. Experimental data from Yu *et al.*³⁷ The left figure shows high-pass filtered pressure data from the experiment, plotted with the oxidizer post length. The experiment starts with stable combustion and a length of 19 cm; as the oxidizer post length is reduced, the system becomes unstable. The experiment returns to marginally stable combustion as the post length approaches 9 cm. The right figure shows the experimental PSD amplitudes for the first longitudinal mode form several test cases. Forward indicates translating from 19 cm to 9 cm. Note that the PSD power is plotted on a linear scale to highlight the variability.

operative on either ends of the highly unstable region. Figure 2 indicates that the gradual transition at short lengths was relatively repeatable and independent of direction of traverse, while the location of the sharp transition at the long-post end was not as repeatable but varied depending on whether the inlet was translated forward, backward, or was held fixed.³⁸ Simulations are conducted at fixed post lengths and are therefore incapable of capturing hysteresis effects due to the translation direction.

To compare the stability behavior in the three regimes, the spectral content at post lengths of 8.9, 14.0, and 19.1 cm is plotted in Figure 3 for the experiment and simulations. The experimental data were sampled at 0.1 MHz and used a sample size of 160 ms, providing a maximum frequency of 50 kHz and a frequency resolution of 6.25 Hz. Computational PSDs were generated using the final 35 ms of the solution. The data were sampled at 10 MHz providing a frequency resolution of 28.5 Hz and a maximum frequency of 5 MHz. Note that two experimental results are shown for the 19.1 cm location which is near the sharp transition from stable to unstable operation. This transition is sensitive to local conditions as noted in Fig. 2(b), and these two experimental realizations contrast extremes between stable and unstable operations at this one condition.

The amplitudes of the peaks from the experiment and the computation should not be directly compared since it is the area under the peak that determines the power associated with it. A direct comparison can be made by integrating under the PSD peaks. The integration is performed using the full-width half-max (FWHM) method,³⁷ and the resulting peak-to-peak pressure amplitudes and the corresponding frequencies for the first three modes are summarized in Table III for both experiments and computations.

In general, the computational-experimental comparisons at the two shorter post lengths, 8.9 and 14.0 cm, are in quite good agreement, while those for the longer post length, 19.1 cm, are less so. In both the experimental and computational results, the moderately stable case (8.9 cm post length) has a relatively low level of instability and only the first two harmonics are clearly distinguishable. Only broad spectral content (if any) is seen for the higher modes. Both the experiment and computation show defined peaks for the first two modes and broad peaks for the higher modes. The unstable post-length case (14.0 cm) reveals a much richer frequency content with multiple sharp peaks in both experiment and computation. The simulation also shows an additional peak between the first and second modes.

The amplitudes of the first three computational modes for both the moderately stable and unstable (post lengths of 8.9 and 14.0 cm) cases as given in Table III are in good agreement with the experiment, with the simulations consistently predicting marginally higher amplitudes at the 8.9 cm

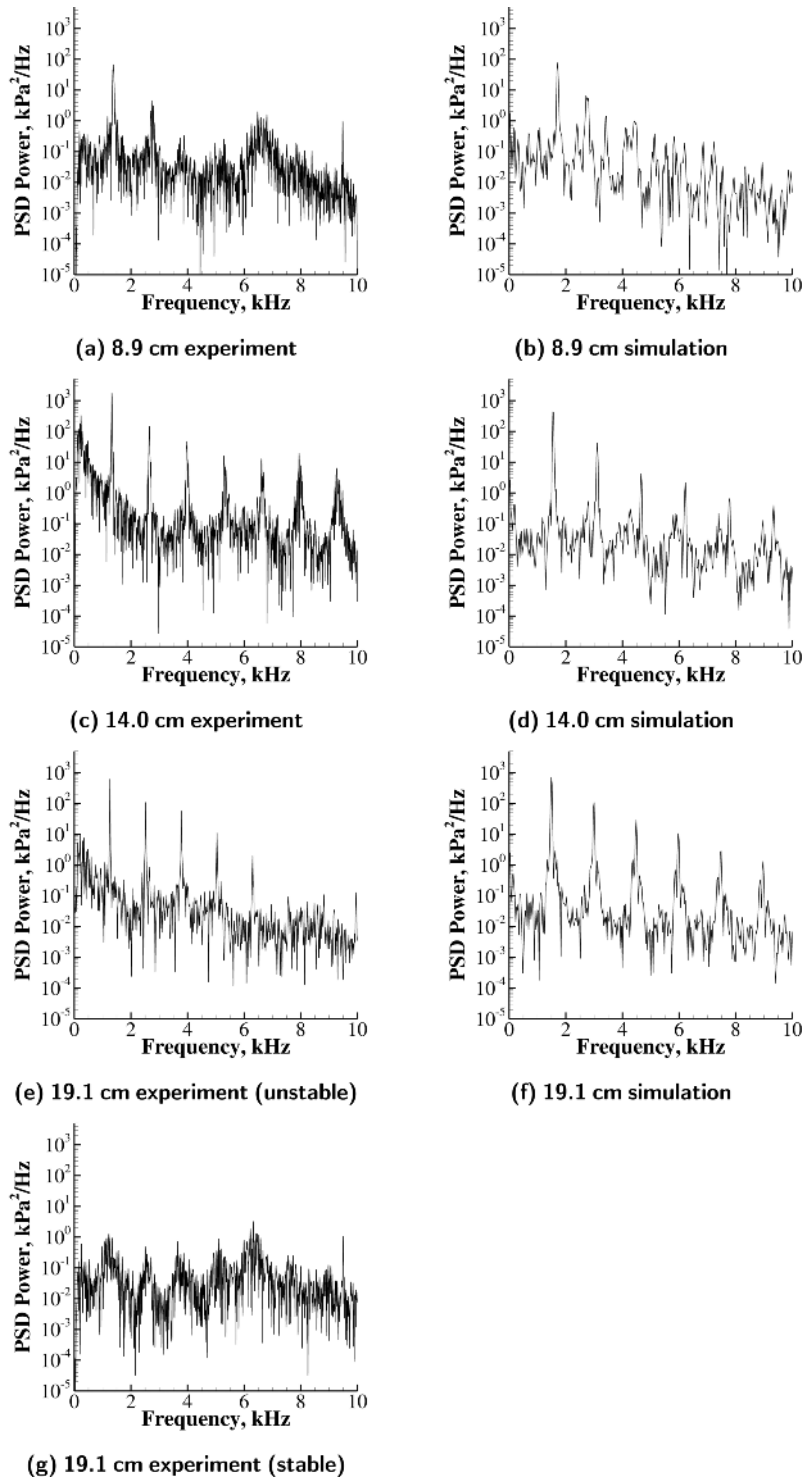


FIG. 3. PSD analysis for the experiment (left) and simulations (right). Point of analysis is on the combustor wall, 37 cm downstream of the back step.

length and marginally lower ones at the 14.0 cm length. Similar agreement with experimental data in the unstable range was also reported by Garby *et al.*²⁶ for a post length of 12 cm. In particular, our peak-to-peak amplitude predictions of 350 kPa at a post length of 14.0 cm agree well with their value of 335 kPa at 12 cm and with the experimental value of 390 kPa. For the unstable 14.0 cm

TABLE III. Frequency and peak-to-peak pressure amplitudes for the experimental and computational operating points.

Oxidizer post length	Mode	Experiment			Simulation			Percent deviation in p'_{ptp} (%)
		f , Hz	p'_{ptp} , kPa	f_i/f_1	f , Hz	p'_{ptp} , kPa	f_i/f_1	
8.9 cm	1	1379	121.17	1.00	1714	129.54	1.00	6.9
	?	2800	40.33	1.63	
	2	2734	5.86	1.98	3428	20.57	1.98	251.0
	3	3882	16.03	2.82	4429	27.57	2.58	72.0
14.0 cm	1	1324	387.15	1.00	1543	349.10	1.00	9.8
	2	2655	89.29	2.01	3114	87.55	2.01	1.9
	3	3979	46.37	3.01	4629	36.25	3.00	21.8
19.1 cm unstable	1	1260	205.27	1.00	1486	395.84	1.00	92.8
	2	2520	88.48	2.00	3000	158.23	2.02	78.8
	3	3780	65.89	3.00	4486	73.25	3.02	11.2
19.1 cm stable	1	1220	15.57	1.00				
	2				
	3	3650	8.10	2.99				

length case, both the experiment and simulation show strong, well defined peaks for the first mode as well as the first several harmonics. Amplitudes of the first three modes show excellent agreement between the experiment and the predictions, in this case, being marginally lower.

The ratios of the frequencies of the higher-order modes to the first mode shown in Table III are in also excellent agreement with the experiment for the 8.9 cm and 14.0 cm cases; both predict near integer multiples of the frequency. The exception to this is the third mode of the 8.9 cm case for which both simulation and experiment predict non-integer multiples; the ratio is however somewhat different between the two. The simulation for the 8.9 cm case also indicates an excited mode at 2800 Hz, which sits between the first and second longitudinal modes. This was not seen experimentally and its source is not clear.

The 19.1 cm length condition is near the sharp transition from stable to unstable where less repeatable experimental results suggest borderline operation, and for this reason, we present two experimental realizations, an unstable one (Figure 3(e)) and a stable one (Figure 3(g)). At the first glance, the computational PSD in Figure 3(f) appears to agree quite well with the unsteady experimental result. Both computation and experiment retain the multi-peak character observed for the mid-post length case, and the peaks and their rate of fall-off are similar. Nevertheless, as noted above, it is not the peaks but rather the integrals under the peaks that are to be compared. The broader computational peaks integrate to levels that are roughly twice those of the experiment, Table III, indicating poorer agreement different than was seen at the two shorter post lengths. One possible reason is that these differences arise because the simulations have yet to transition to stable at this post length. Additional possibilities are discussed in Sec. IV, where it is also noted that the driving mechanisms in the 14.0 cm and 19.1 cm computations are different despite their similar amplitudes.

For all post lengths and acoustic modes, the predicted frequencies are proportionally higher than the experimental values. The primary reason is that the experimental heat loss was not accounted for in the simulations. The experiments were conducted in a heat-sink chamber that extracted a significant amount of the energy from the flow resulting in a chamber temperature substantially lower than the adiabatic flame temperature with an accompanying reduction in the sound speed. With adiabatic wall conditions, the chamber temperature in the simulations is approximately equal to adiabatic flame temperature, and the corresponding chamber pressure was 1.5 MPa as compared to the experimental value of 1.3 MPa. (A similar calculated chamber pressure was reported by Garby *et al.*²⁶) For a chamber with a choked throat, a 15% higher chamber pressure corresponds to a 15% over-prediction of the sound speed with a similar effect on the acoustic

frequencies. Previous calculations with and without heat flux^{28,58,59} of the generically similar experiment by Pal *et al.*,⁴⁷ in which the wall heat flux was measured, have also noted a similar reduction in chamber temperature and acoustic speed. In addition to the heat loss, a second factor that leads to increased chamber temperatures and sound speeds is the partial dissociation in the simplified thermochemistry. Note that the higher sound speed makes the chamber appear acoustically shorter than the experiment but is not expected to change the instability mechanisms.

III. IDENTIFICATION OF INSTABILITY MECHANISMS

In this section, we introduce three phenomena related to the instability behavior observed in the CVRC. First, the relative timing between the resonant pressure field and flow phenomena is clearly important in elucidating instability mechanisms. Accordingly, we start by estimating the traverse times of pressure pulses (compression wave fronts) in the combustor and oxidizer post to describe the conditions at the exit of the ox-post at the time a pressure pulse reflected from the combustor nozzle returns to the back step. The second phenomenon considered is increased mixing due to vorticity production by baroclinic torque, while the third is the transitory migration of triple flames.

A. Pulse timing

Table IV lists estimated mean values for the velocity and sound speed along with the relevant lengths of the combustor and oxidizer post. These quantities are then used with simple acoustic theory to estimate the travel times of pressure pulses to help anchor the events in the simulations. The travel times are estimated using

$$t = t^{\rightarrow} + t^{\leftarrow},$$

$$t = \left(\frac{L}{u + c} \right) + \left(\frac{L}{c - u} \right), \quad (1)$$

where L is the length, c is the sound speed, and u is the mean velocity. The downstream travel time is denoted by t^{\rightarrow} and the upstream travel time is denoted by t^{\leftarrow} . The effect of mean flow is considered because of the high local Mach number in the oxidizer post. For consistency, this assumption, although less important, is also carried through for the combustor analysis.

As the oxidizer post length is varied, the wave transit times in the post change while those in the combustor remain constant. Examples of half- and quarter-wave resonators are shown in Figure 4. In each case, a pressure pulse starts at the back step. For the $1/4$ resonator, the wave in the left tube makes a round trip back to the starting point while the wave in the right tube makes it only to the downstream end. In the $1/2$ wave resonator case, the waves in both tubes return to the starting point in the same amount of time. The only one ox-post length that presents a pure resonance with the chamber is the $1/2$ -wave resonator, and the pressure field is dominated by the combustor acoustics. If we consider a cycle to be the time, it takes a pressure pulse to travel from the back step to the nozzle

TABLE IV. Approximate pulse times from a simple acoustic analysis.

Parameter	Region			
	Combustor	8.9 cm post	14.0 cm post	19.1 cm post
L , cm	38.1	8.89	13.97	19.05
u , cm/ms	16.0	22.0	22.0	22.0
c , cm/ms	120.0	69.0	69.0	69.0
t^{\rightarrow} , ms	0.28	0.10	0.15	0.21
t^{\leftarrow} , ms	0.37	0.19	0.30	0.40
t , ms	0.65	0.29	0.45	0.61
$f = c/2L$, Hz	1574	3880	2470	1811

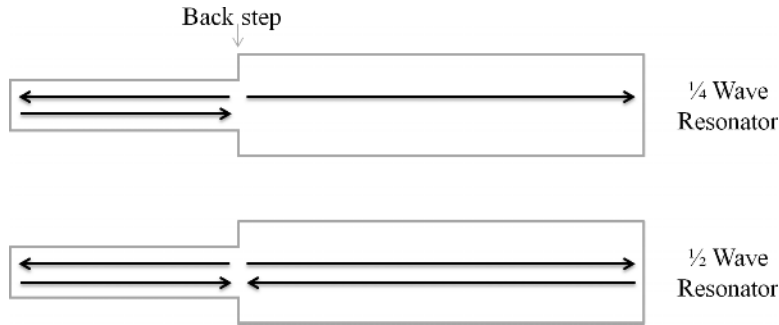


FIG. 4. Pictorial description of a 1/4 wave and 1/2 wave resonators.

and then returns to the back step ($t = 0.65$ ms); the conditions at the exit of the oxidizer post at the end of the cycle will be different for each ox-post length. The long ox-post (19.1 cm case) is the closest to a resonant condition, where the pressure pulses traveling up and down the combustor and ox post will meet at the back step. The short ox-post is close to a 1/4-wave resonator. Considering that a cycle starts and ends with high pressure at the back step and using the estimated transit times listed in Table IV, Figure 5 shows the pulse movements for a single cycle for the three cases.

When a pulse traveling in the ox-post is reflected from the inlet and returns to the back step when the pressure in the combustor is low, a strong positive pressure gradient exists near the exit of the ox-post. This pressure gradient forces any fuel in the shear layer outward into the recirculation region where hot gas is present. This event has the potential to cause ignition near the back step. In the case where the pressure at the back step is not low at the time of the returning pulse, this phenomenon does not appear. For the 14.0 cm length, the return time of the reflected pulse coincides with the point in the cycle where the pressure at the back step is lowest. This is not the case for the 8.9 cm or 19.1 cm lengths. Instead, for the 8.9 cm case, the return wave coincides with the falling chamber pressure before significant fuel can accumulate. In the 19.1 cm case, the wave returns during a local rise in pressure.

B. Baroclinic torque

Increased mixing in a non-premixed flow can give rise to higher combustion heat release. One source of increased mixing is an increase in vorticity in regions of non-premixed flow. To understand the sources of vorticity, we look into the vorticity transport equation. For compressible flow with no body forces, the equation describing vorticity is

$$\frac{d\boldsymbol{\omega}}{dt} = (\boldsymbol{\omega} \cdot \nabla) \mathbf{u} - \boldsymbol{\omega} (\nabla \cdot \mathbf{u}) + \frac{\nabla \rho \times \nabla p}{\rho^2} + \nabla \times \left(\frac{\nabla \cdot \boldsymbol{\tau}}{\rho} \right). \quad (2)$$

The term of interest is the baroclinic torque, which is the third term on the right hand side. This term represents the generation of vorticity due to misalignments in the gradients of density and pressure.⁶⁰ The region near the fuel injection is home to strong density gradients where the cooler and denser fuel ($\rho_0 = 10.2$ kg/m³) is adjacent to the warmer and lighter oxidizer ($\rho_1 = 4.3$ kg/m³). Consider the sketch of a shear layer shown in Figure 6. As the pressure pulse moves (upstream or downstream) through the oxidizer post, the pressure gradient is aligned with the axial direction and there is a strong radial density gradient. This configuration will result in a generation of vorticity in the circumferential direction. Vorticity generation in this region can promote mixing of the oxidizer and fuel resulting in portions of the flowfield that are partially premixed. These partially premixed regions can result in combustion taking place upstream of the back step. Recent work by Ghosh and Yu suggested that baroclinic torque in shear coaxial injectors might be a link between small-amplitude acoustic disturbances and flame dynamics.⁶¹

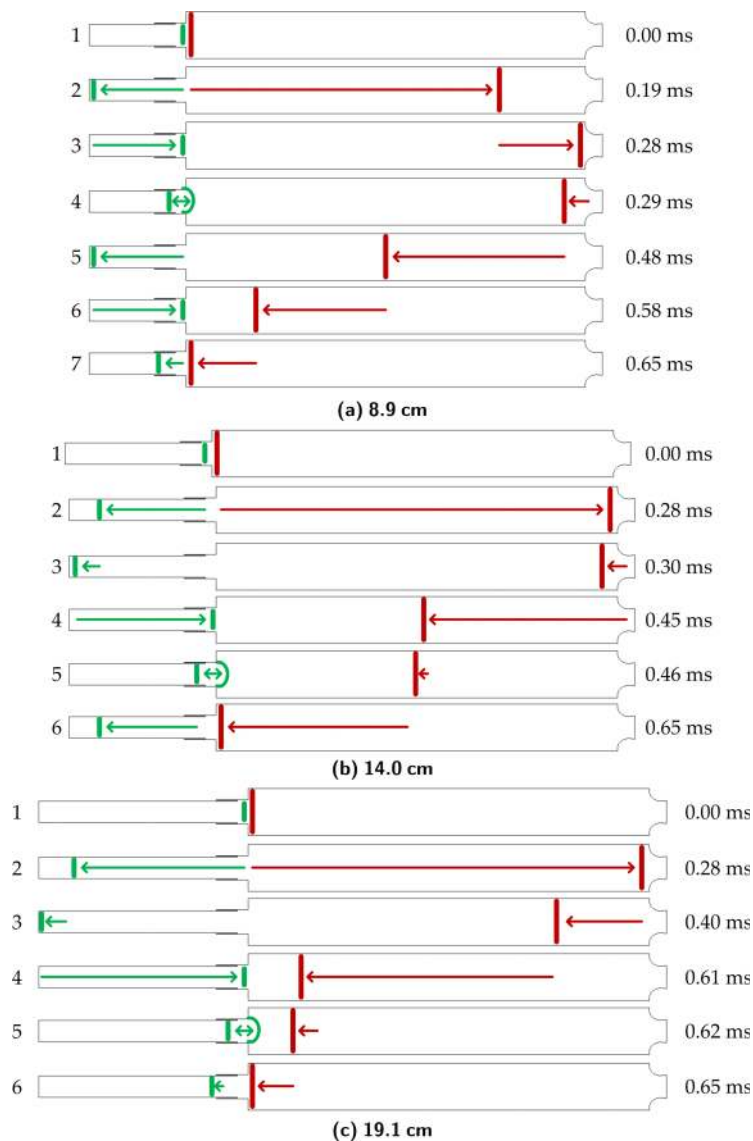


FIG. 5. Acoustic wave events. Times to the left are the elapsed time of the cycle.

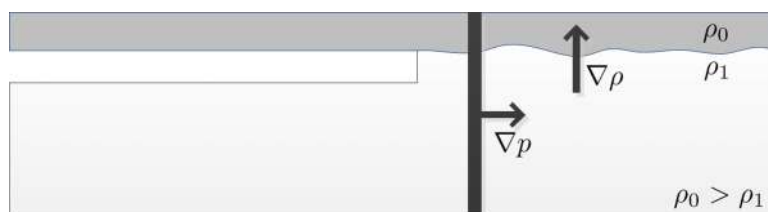


FIG. 6. Shear layer showing the dense fuel against the wall and the less dense oxidizer in the core.

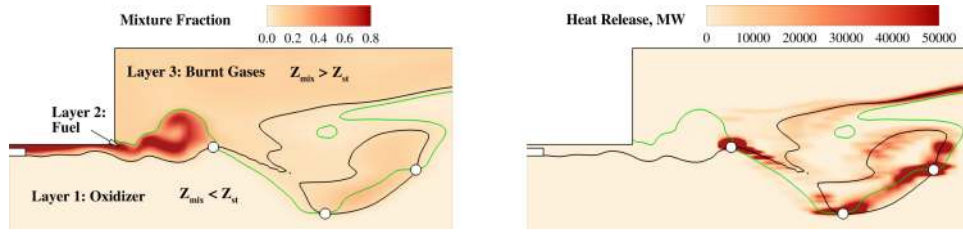


FIG. 7. Triple flame structure; three triple points are identified (white circles) at the intersection of the green and black lines. In both plots, the green line is a $T = 2000$ K contour and the black line is the stoichiometric mixture fraction, Z_{st} .

C. Triple flame

A triple flame occurs at the intersection of a leading fuel rich premixed flame, a leading fuel lean premixed flame, and a trailing diffusion flame.⁶² This point (or line in three dimensions), also referred to as a triple point, coincides with regions of intense heat release. Identification of the triple flame is possible by exploring the local mixture fraction. The mixture fraction is defined as⁶³

$$Z = \frac{\nu_{st} Y_{CH_4} - Y_{O_2} + Y_{O_2}^0}{\nu_{st} Y_{CH_4}^0 + Y_{O_2}^0}, \quad (3)$$

where $n_{st} = 4.0$, $Y_{CH_4}^0 = 1.0$, and $Y_{O_2}^0 = 0.4235$ for the present configuration. Y_{O_2} and Y_{CH_4} are the local mass fractions of oxygen and methane, respectively. Also relevant is the stoichiometric mixture fraction, $Z_{st} = 0.095739$. Figure 7 shows snapshot of the triple flame structure from the present simulations. In addition to the stoichiometric mixture fraction (shown by the black line), the approximate location of the flame front (designated by the $T = 2000$ K isoline shown in white) is also illustrated. There are three distinct layers comprising oxidizer, fuel, and the burnt gases in the recirculation region. Garby *et al.* also deduced the existence of the triple flame structure using a simulation for an unstable 12 cm length. They suggest that no burning occurs upstream of the back step and the hot recirculation gases are responsible for heating the mixture of unburnt fuel and oxidizer. They note that the chemistry is not fast enough to anchor the flame at the injection point, and the flame is instead anchored at the dump plane by the hot burnt gases in the recirculation region.²⁶ Results in the present work find that the mechanism at play in the unstable case is more complex and dynamic. The triple flames move throughout the head-end of the combustor. They are extinguished and reform regularly and in some instances can be found upstream of the back step.

IV. CYCLE ANALYSIS

Sections IV A–IV C look at the behavior during a single cycle for each of the three stability regimes. In each case, we try to elucidate how the three phenomena discussed above—pulse timing, baroclinic torque, and the triple flame—combine to result in stable or unstable combustor response. Figure 8 shows the cycles that will be examined for each case. A cycle starts with high pressure at the head end and continues until the head end again experiences a high pressure. Start and end

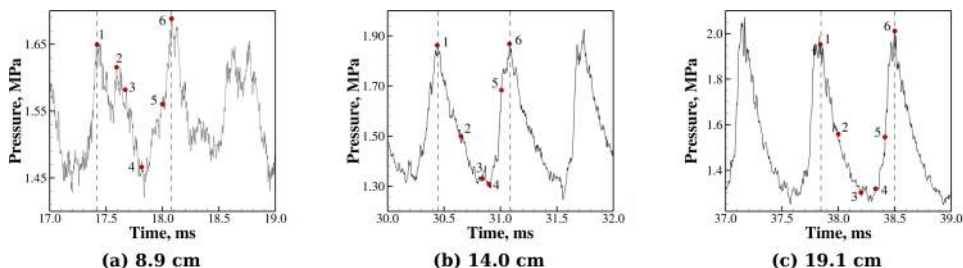


FIG. 8. Pressure plots of the cycle of interest for each configuration. Note that the pressure scales are different in each figure.

times of the cycle are marked with vertical lines in the figure. Six points are marked on each cycle; these points have been judiciously chosen to highlight the events discussed in Sec. III as well as illustrating the overall unsteady behavior. The results for the 14.0 cm length are presented first; the remaining two lengths build on the 14.0 cm results.

A. 14.0 cm oxidizer post length

We start with the unstable case which corresponds to the 14.0 cm oxidizer post length. The corresponding time varying pressure is shown in Figure 8(b). Although the instantaneous flow-field is three-dimensional, sufficient understanding and improved visualization can be realized from two-dimensional slices. Figure 9 shows a series of plots for the six points in the cycle marked in Figure 8(b). The domain shown for this and succeeding cases is limited to 5 cm upstream and 13 cm downstream of the back step. The plots on the left are of the CH_4 contour, and superimposed on the contour are lines colored with the static pressure. Plots on the right are of the combustion heat release contour; two lines are superimposed on the contour, the white line signifying a temperature of 2000 K and a black line marking the stoichiometric mixture fraction allowing for triple flame

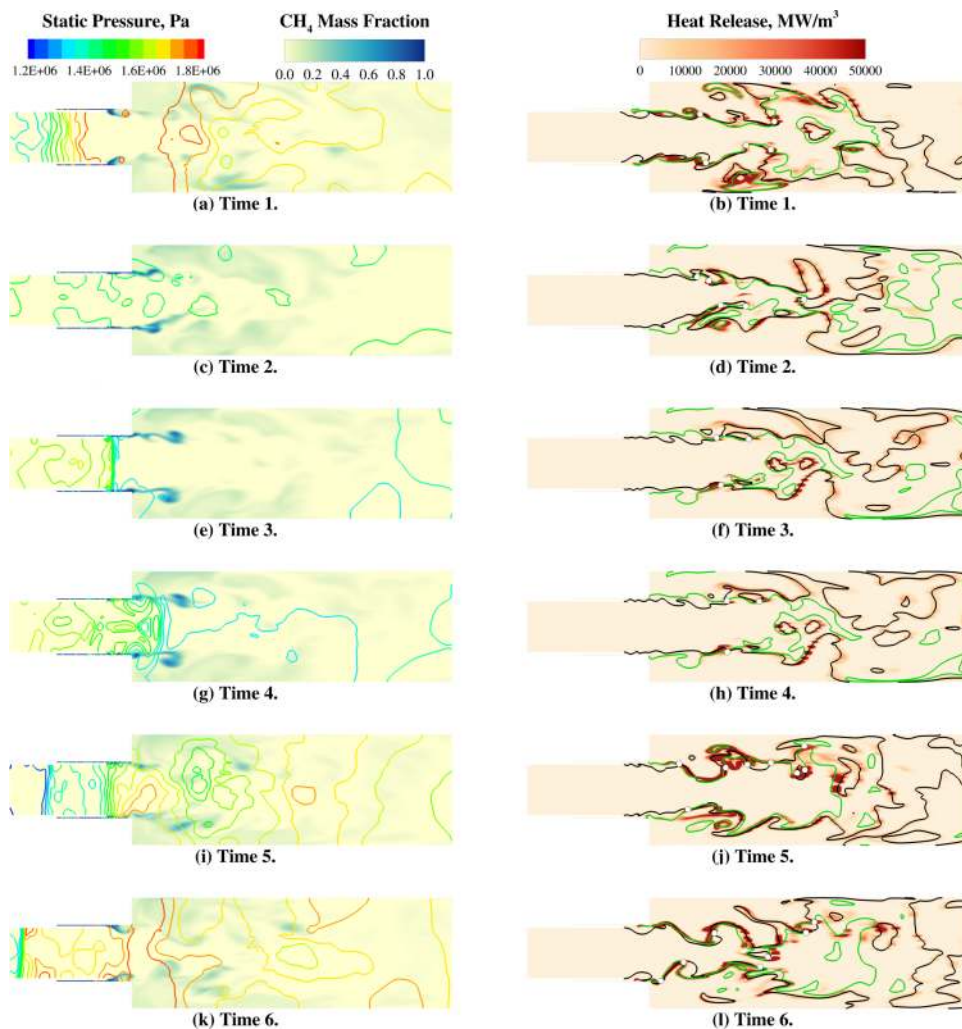


FIG. 9. Cycle snapshots for 14.0 cm. Left images: contour is colored with CH_4 mass fraction; lines are colored with static pressure. Right images: contour is colored with combustion heat release, the green lines are a temperature iso-line for $T = 2000$ K, and the black line represents the stoichiometric mixture fraction. Triple points are marked with white circles. Contour levels are consistent for all times.

identification. The temperature line serves to demarcate the burnt and unburnt gases. Combustion along the temperature line is due to a premixed flame; this occurs in the region where fuel and oxidizer are mixed and have warmed adjacent to the burnt gases, while that along the stoichiometric line represents a diffusion flame.²⁶ A quick preview of the snapshots of CH_4 mass fraction and heat release shows that the flame goes through a cycle of attachment, detachment, and reattachment to the back step. In the following paragraphs, the snapshots are described in some detail to explain how the relative timing of the resonating pressure pulses in the ox-tube and the combustor combines to affect the flame dynamics and, in turn, stimulates the high-amplitude pressure oscillations at this geometric condition.

Starting at time 1, the cycle has just begun and the pressure in the head-end of the combustor is decreasing from its maximum value. The pressure contours indicate two pulses moving away from the back step in opposite directions, one moving upstream in the oxidizer post and a second moving downstream in the combustor. The CH_4 mass fraction shows a disruption in its flow near injection, the result of the local pressure pulse that has moved upstream in the oxidizer post. Consequently, there is a disruption in the combustion process as well, which is responsible for the non-steady burning associated with instability. The combustor is largely devoid of any significant concentrations of CH_4 with the exception of an annular region near the wall close to the reattachment point of the primary recirculation region. Notably, there is heat release upstream of the back step adjacent to the wall in the region where CH_4 is absent. In the combustor, significant heat release is confined to the region near the temperature line and the annular pocket of CH_4 near the reattachment point. Triple points are located away from the back step.

As the cycle progresses to time 2, the pressure near the back step continues to drop. The disruption in the combustion process continues, and there is little evidence of combustion heat release in the region near the back step. The distribution of CH_4 shows that there are significant concentrations of CH_4 downstream of the back step in the shear layer indicating the accumulation of unburnt fuel in the combustor. Also, note that there is no longer any combustion upstream of the back step, and there is a high concentration of CH_4 lining the wall. This region is no longer sufficiently mixed to support combustion. The region where the fuel is located is lower in temperature; the stoichiometric line and temperature line are further apart in regions where there is no burning. Also, note that unlike the previous time, the burning here is concentrated in the center of the combustor and not near the walls. The triple point holds roughly the same axial position as the previous time.

Time 3 sits in the trough (local expansion) of the cycle, just before the reflected pressure pulse in the oxidizer post returns to the back step. Similar to time 2, there is significant CH_4 in the combustor along the shear layer, and unburnt fuel is being recirculated and accumulated near the combustor wall. The heat release contours show that these regions of high fuel concentration are not yet burning due to poor mixing. The triple points have moved further downstream along with the significant heat release further indicating the lack of combustion near the injector.

In the oxidizer post, the reflected pressure pulse is just passing the fuel collar and moving downstream towards the back step. The pressure pulse passing through the fuel injection region generates vorticity because of a non-zero baroclinic torque. This begins to wrinkle the mixture fraction line in Figure 9(f) and creates a partially premixed region upstream of the back step allowing combustion to take place in this region at a later time. The effect of the baroclinic torque for all three lengths will be contrasted following the cycle analysis.

When the pressure pulse passes the back step and moves into the combustor, there is a spike in pressure visible in the wave trough (Figure 8(b)). A plot of the flowfield at this time is shown in Figure 10. This figure shows strong pressure gradients that expand radially outward and push the CH_4 rich fluid into the hot recirculating gases immediately downstream of the back step. Although not shown, there is no heat release occurring in the region of high CH_4 concentration.

Time 4 in the cycle represents the final low pressure point. Notice there is significant wrinkling in the mixture fraction line upstream of the back step due to the baroclinic mixing generated by the pressure pulse. Moreover, the flame now reappears at the combustor head-end and is attached to the back step, indicating that local re-ignition has occurred. This is possibly allowed by the fuel being pushed into the recirculation region by the high-pressure gradient in the previous step. The recirculation region has hot combustion products, and this parcel of fuel and oxidizer ignites very

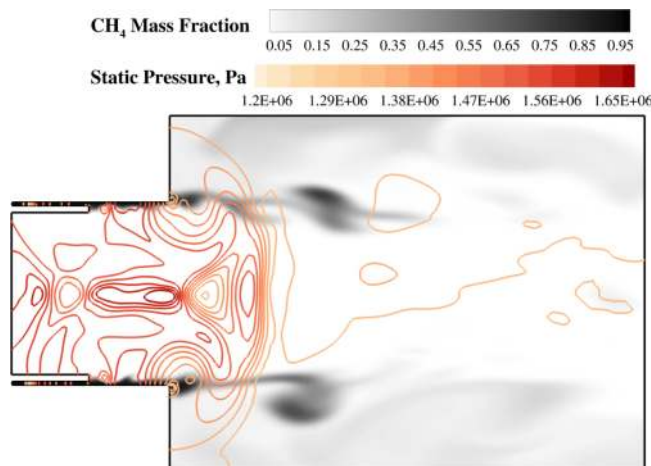


FIG. 10. Snapshot at the trough of the wave just past time 3, 14.0 cm post. Close up showing the radial displacement of the fuel near the back step. Contour is colored with CH_4 mass fraction; lines are colored with static pressure.

close to the wall. The flame then propagates upstream toward the back step and ignites the partially premixed flow created by increased baroclinic torque due to the previously passing pressure pulse. In some cases, the flame even propagates into the premixed mixture upstream of the back step. Overall, we refer to this mode of reignition as the “post-coupled” mechanism since the returning pressure wave in the oxidizer post generates the fuel-oxidizer mixing that is responsible for the combustion.

There is a large increase in pressure as we move from time 4 to 5, almost 0.4 MPa due to the ignition of methane near the back step observed in the previous time instance. The pulse in the combustor is on its way back to the back step but has not yet arrived, and the pressure pulse in the oxidizer post largely dissipates after expanding into the combustor between times 3 and 4.

At time 5, the pressure wave in the combustor has moved upstream to the recirculation region. The associated baroclinic torque leads to increased mixing and subsequent combustion of the unburnt fuel that has accumulated in the chamber because of the earlier disruption in the combustion process. In turn, the increased combustion heat release leads to an even greater increase in the pressure between times 5 and 6.

At time 6, the high-pressure pulse from the local combustion has again begun to propagate upstream in the oxidizer post. As shown by the elevated concentrations of methane away from the wall, the fuel flow becomes detached from the wall in the region upstream of the back. The adverse pressure gradient caused by the pulse and the increased premixing during times 4 and 5 has allowed the flame to propagate upstream from the back step. The combination of this burning and the flow disruption will act to starve the combustor of fuel at the beginning of the next cycle. This sets up the flame detachment event that occurs between times 1 and 2, causing the heat release to again move downstream away from the back step, and the cycle is then poised to repeat.

B. 8.9 cm oxidizer post length

The computations and experimental results show that the 8.9 cm oxidizer post length is marginally stable, having peak-to-peak amplitudes of about 150 kPa compared to the 600 kPa amplitudes of the 14.0 cm case. A pressure trace for the cycle of interest was shown in Figure 8(a). The lower amplitudes result in cycles that are not as regular, but the chosen cycle is representative of the overall limit cycle behavior.

A preview of the plots in Figure 11 highlights several key differences to the results presented for the 14.0 cm case. The most notable difference is that both fuel injection and heat release are more continuous. The flame remains anchored to the back step and does not propagate upstream into the premixing region. Importantly, the fuel interruption event that occurred at time 1 (or time 6)

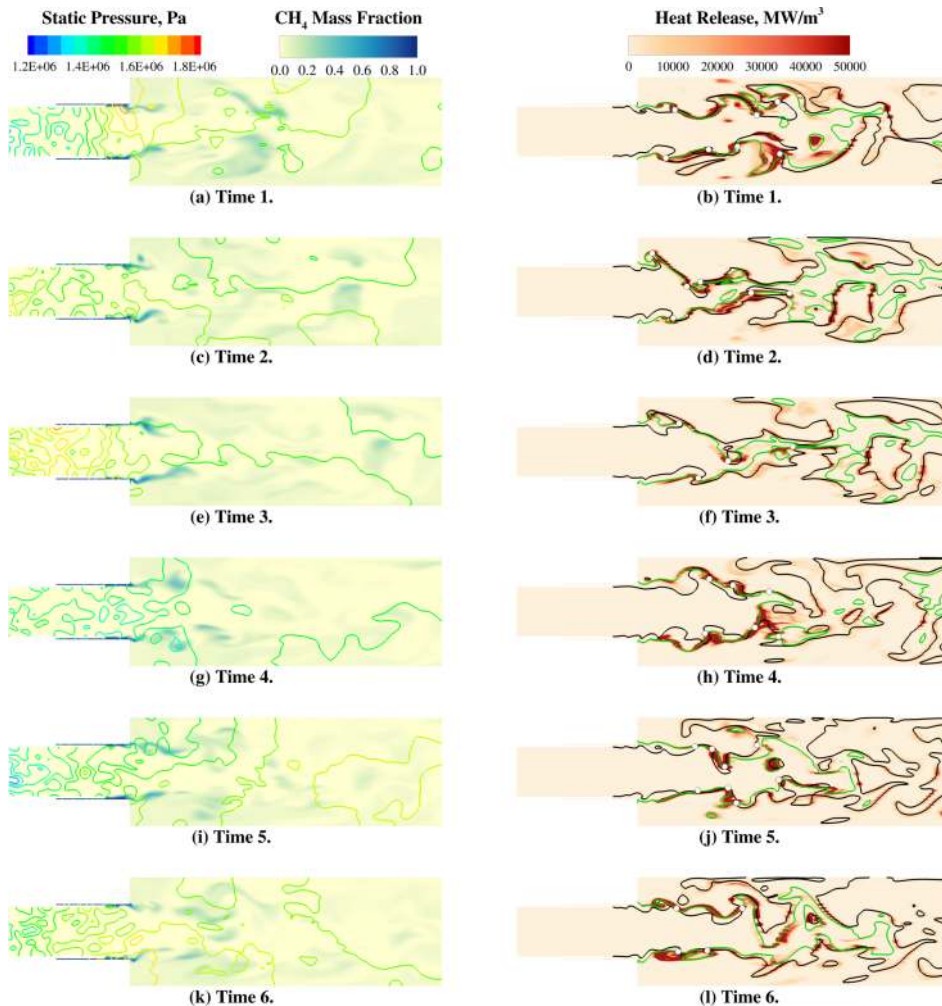


FIG. 11. Cycle snapshots for 8.9 cm. Left images: contour is colored with CH_4 mass fraction; lines are colored with static pressure. Right images: contour is colored with combustion heat release, the green lines are a temperature iso-line for $T = 2000$ K, and the black line represents the stoichiometric mixture fraction. Triple points are marked with white circles. Contour levels are consistent for all times.

is absent. The heat release still couples with the pressure to some degree, but since there is no clear interruption in the combustion, the large reignition at time 4 that resulted from the accumulation of unburnt fuel is absent. Significantly, less premixing occurs upstream of the back step, as indicated by less wrinkling in the lines of fuel mass fraction. The pressure pulse that occurred near the ox-post exit at time 3 in the 14.0 cm case is also absent and unburnt fuel is not pushed radially outward behind the back step.

Snapshots for the cycle are shown in Figure 11. Note that for this case, the pressure amplitudes are much lower and tend to show more variability in the radial direction. There is no heat release upstream of the back step along the wall, and there is no disruption to the fuel flow from the high-pressure pulse moving through the oxidizer post. Triple points are located downstream of the back step.

At time 1, there is an initial decay in pressure, which is the result of the acoustic waves moving away from the back step towards the nozzle and oxidizer injector. Time 2 shows a second relative peak in the pressure signal near the back step, a result of continued combustion in the region. Without the fuel interruption event, the combustion continues and the pressure briefly increases. At time 2, there is some evidence of unburnt fuel in the combustor near the back step, but for the majority of the combustor, there is a diffusion flame positioned along the $T = 2000$ K line. In the

instant shown, this flame extends upstream almost reaching the back step. In this instance, a triple point is located near the back step (top of the figure).

The pressure pulse in the oxidizer post returning to the combustor is relatively non-eventful in this case, occurring at point 3. The travel time for the wave in the short ox-post is less than half the travel time in the combustor (see Table III), and the pulse is weakened due to destructive interference with the local expansion at the head end of the combustor. The weaker pressure gradient results in less vorticity generated from the baroclinic torque and less premixing of the fuel and oxidizer in the shear layer upstream of the back step as indicated by the relatively smooth mixture fraction line. It is possible that the decreased premixing prevents combustion from occurring upstream of the back step, which was seen to be a key event that interrupted the fuel flow in the 14.0 cm case. There is heat release close to the back step which extends downstream along the $T = 2000$ K line. Recall that in the 14.0 cm case, the interruption of fuel caused the flame to detach from the back step as the pressure decreased to the low point of the cycle.

Time 4 is the low pressure point of the cycle. Heat release continues near the back step with combustion again primarily taking place along the $T = 2000$ K line which is offset from the stoichiometric mixture fraction line. Combustion remains absent upstream of the back step as the pressure increases. At time 5, the returning high pressure pulse is visible at the downstream end of the viewing region.

The highest heat release occurs when the head end of the combustor is at the maximum pressure point in the cycle. The flame is again primarily located along the $T = 2000$ K line with peak heat release near the intersection of the temperature and mixture fraction lines. Without combustion and without fuel disruption upstream of the back step, the fuel can flow continuously into the combustor for the next cycle, and the reignition event is eliminated. This continuous combustion heat release is clearly well correlated with the lower amplitudes of pressure oscillation leading to relatively stable combustion response.

C. 19.1 cm oxidizer post length

The 19.1 cm length shows considerable variability in the experiments with both stable and unstable combustions being observed during different tests. The simulation for the 19.1 cm case predicts higher pressure oscillation amplitudes (see Figure 8(c)) than those observed in the experiment. There are numerous possible reasons for this disagreement, but perhaps, the most important is the fact that the transition at the long ox-post side is quite sharp, and there is considerable variability in the length at which it occurs (as seen earlier in Figure 2). In particular, different experimental conditions (direction of traverse, wall material, etc.) change the transition length by approximately three centimeters. This variability makes back-to-back comparisons between computations and experiment challenging, and it is likely that simulations would predict transition at somewhat different post lengths than those observed in the experiment. With regard to transition length, the simple one-step global reaction/laminar flame model is an obvious area that requires improvement. In this regard, preliminary calculations based upon a thickened flame approximation⁵⁷ have shown little change in the predictions although other turbulent combustion models might have more impact.

A different alternative is the impact of the adiabatic wall condition. The experiment has shown that wall conditions have a decided impact on the transition location. This is most likely not because of a change in instability mechanisms but rather because of a change in the tuning characteristics of the chamber. The adiabatic wall condition increases the resonant frequency and changes the timing between the pressure field and associated flow events. The increased sound speed noted earlier changes the effective post to chamber length ratio, which would be expected to change the transition length while having little effect in the broad unstable region where conditions are only mildly dependent on post length. Preliminary calculations for a 22 cm post continue to show amplitudes like those at the 19.1 cm case suggesting transition has not yet occurred at this length. Finally, we note that in addition to its global effect on the acoustics, the near-wall extraction of heat in the experiment may have a local effect on ignition and flammability, whereas the hot walls of the simulation may promote these effects.

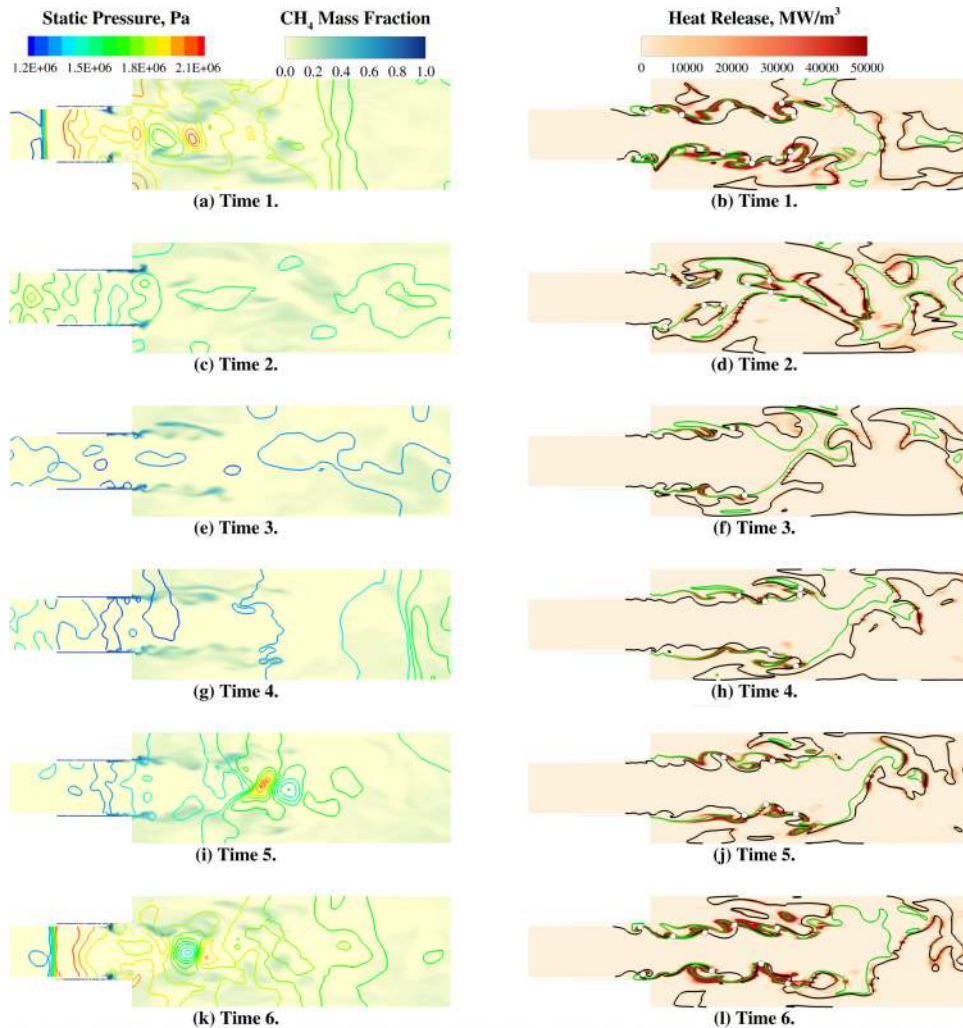


FIG. 12. Cycle snapshots for 19.1 cm. Left images: contour is colored with CH_4 mass fraction; lines are colored with static pressure. Right images: contour is colored with combustion heat release, the green lines are a temperature iso-line for $T = 2000$ K, and the black line represents the stoichiometric mixture fraction. Triple points are marked with white circles. Contour levels are consistent for all times.

Despite the differences between experiment and simulation, it is interesting to compare the 19.1 cm case with the 8.9 cm and 14.0 cm cases. A preview of Figure 12 shows similarities and differences compared to the other cases. Like the stable 8.9 cm case, and unlike the unstable 14.0 cm case, the heat release is generally continuous and stays attached to the back step most of the time, although at times it is weakly attached. Compared to the 14.0 cm case, there is relatively little CH_4 that recirculates to the combustor wall and upstream toward the back step; there is also less heat release occurring in those areas. Most of the time, the fuel mass fraction is relatively continuous along the shear layer, similar to the stable 8.9 cm case.

Similar to the 14.0 cm length, the beginning of the cycle at time 1 shows disrupted fuel flow and combustion upstream of the back step. The pressure pulse that moves into the oxidizer post from the combustor is responsible for pushing the incoming fuel backwards and away from the wall. The stoichiometric line moves away from the wall, allowing the flame to propagate upstream behind the displaced region of high fuel concentration. A triple point (line) is seen upstream of the back step, which was not observed for either the 8.9 cm or 14.0 cm length.

As the pressure decreases at time 2, the CH_4 reattaches to the wall upstream of the back step, and the flame and triple point move downstream. This is due to the flow disruption and depletion of

partially premixed fluid in the region. Fuel begins to accumulate at the dump plane. By the trough of the wave, time 3, there is significantly less heat release in the combustor, and the shear layer has a high concentration of CH_4 . CH_4 is also found in the recirculation region. Heat release is primarily taking place along the temperature iso-line (premixed flame).

The 19.1 cm ox-post nearly acts like a half-wave resonator of the combustor, and the reflected waves in each segment nearly coincide at the back step. Thus, the reflected ox-post wave does not appear in the trough of the combustor wave as it did for the 14.0 cm case. Time 4 is just before the pressure in the combustor begins to rise. In the combustor, CH_4 concentrations are elevated. These fluid parcels with elevated CH_4 concentration can be found further downstream than what was observed in either the 8.9 cm or 14.0 cm case. The fuel in the shear layer is warmed by the adjacent flow of hot recirculating gas. This is evident by the stoichiometric line sitting outside the temperature iso-line. The warmed fuel begins to combust producing an annular ring of significant heat release. At time 5, there is a localized pressure rise located at the center of the burning annulus (Figures 12(i) and 12(j)). Note that at this late stage in the cycle, the flame is weakly attached to the back step and there is still no burning upstream of the back step. The oxidizer post wave returns, but its return is overshadowed by a large pressure rise in the combustor from the downstream heat release. This mechanism is referred to as the “vortex convection” mechanism whereby the reignition takes place downstream unlike the “post coupled” mechanism where the returning oxidizer post wave triggered the combustion.

At the end of the cycle, there is substantial heat release along the shear layer extending back into the oxidizer post. Again, note the presence of the triple point near the fuel injection. The fuel consumed near the injector will give rise to the starvation event for the next cycle. For the 19.1 cm case, reignition after the starvation event is due to fuel in the combustor warming next to the recirculation gases downstream. For the 14.0 cm case, the reignition was due to the returning wave pushing the fuel into the recirculation gases at the back step. This suggests that the effect of wall temperature in this region may be important in accurately predicting the stability at this length.

D. Baroclinic torque

Vorticity generation in the shear layer upstream of the back step through baroclinic torque occurs when a pressure pulse passes through the region. Increased vorticity leading to increased mixing generates a partially premixed region of fuel and oxidizer upstream of the back step that is susceptible to combustion. Combustion upstream of the back step is a precursor to the fuel starvation event, which ultimately leads to the instability. Figure 13 shows the baroclinic torque in the vicinity of the back step for the three oxidizer post lengths. The snapshots are taken just after the oxidizer pressure pulse passes through the region. Notice that in the 8.9 cm case, which does not show the starvation event, there is significantly less vorticity being generated compared to the

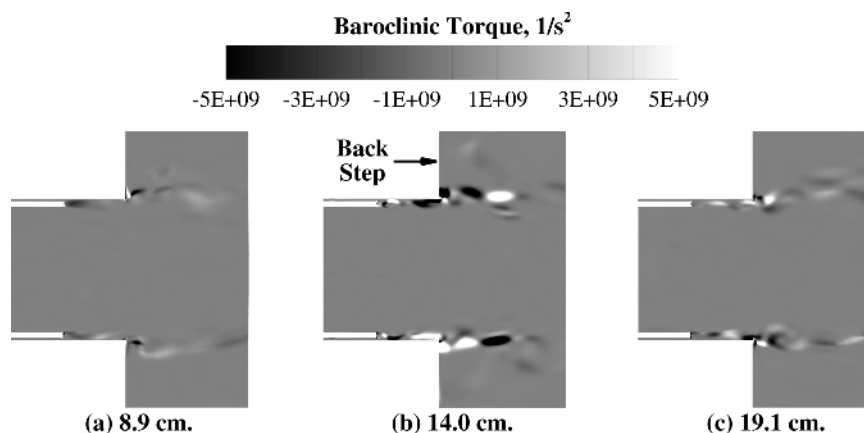


FIG. 13. Baroclinic torque near fuel injector. Snapshot shows the time just after the pressure pulse passes by the region. The region shown extends 2 cm upstream and downstream of the back step; the full radial extent is shown.

14.0 and 19.1 cm cases which do exhibit the starvation event. The presence of the partially premixed region upstream of the back step allows combustion to take place in this region. Recall that in the case of the 8.9 cm length, no combustion was found upstream of the back step.

E. Rayleigh index

As a final assessment of the effect of post length on instability, we compare Rayleigh indices¹ for the three different post lengths. The Rayleigh index provides a measure of the correlation between pressure and combustion heat release oscillations. To obtain local values of the index over the active combustion area, we integrate over each individual cell volume using the mathematical expression

$$\mathcal{R}(\mathbf{x}_i) = \frac{1}{T} \int_{t_0}^{t_0+T} p'(\mathbf{x}_i, t) \dot{q}'(\mathbf{x}_i, t) dt, \quad (4)$$

where p' and \dot{q}' are the fluctuating pressure and heat release, respectively, T is the period of integration, and t_0 is the start time. Representative results are summarized in Figure 14. For all three post lengths, areas of non-zero Rayleigh index appear in the region downstream of the back step. Positive values (indicating regions where the pressure and heat release are in phase and amplify the instability) arise in the shear layer, while negative values (representing out of phase regions which damp the instability) appear in the recirculation region, and for the two longer post length cases, near the centerline. Surprisingly, the Rayleigh index downstream of the back step suggests the relatively stable 8.9 cm case has the strongest driving (although it also appears to have stronger regions of damping), while the highly unstable 14.0 cm length exhibits the weakest growth.

In the small region upstream of the back step, where combustion was observed for the two longer post-length cases, the 8.9 cm case shows neither positive nor negative Rayleigh indices in agreement with the previously noted absence of combustion upstream of the back step for this case. The Rayleigh index for the 14.0 and 19.1 cm cases is relatively strong in this region and extends nearer to the splitter plate in the latter case, possibly explaining the reasons for the stronger instability in these two simulations. Overall, the Rayleigh index results, which would be somewhat puzzling if the Rayleigh mechanism is considered to be the only mechanism, suggest that other driving and damping mechanisms are also at play. Nicoud and Poinso⁶⁴ suggest, for instance, that it is the fluctuating energy equation (which accounts for entropy) not the standard acoustic energy equation that should be used for the analysis of turbulent combustion. They also state that the Rayleigh index must be compared against the acoustic losses at the boundary, and we suggest here that there are probably other driving and damping mechanisms to compare with as well.

F. Dynamic mode decomposition (DMD)

As a final comparison with experiment, we briefly present the results of a DMD. DMD is a modal decomposition technique proposed by Schmid to look at the dynamics associated with engineering problems.⁶⁵ DMD is similar to the proper orthogonal decomposition (POD) technique.⁶⁶

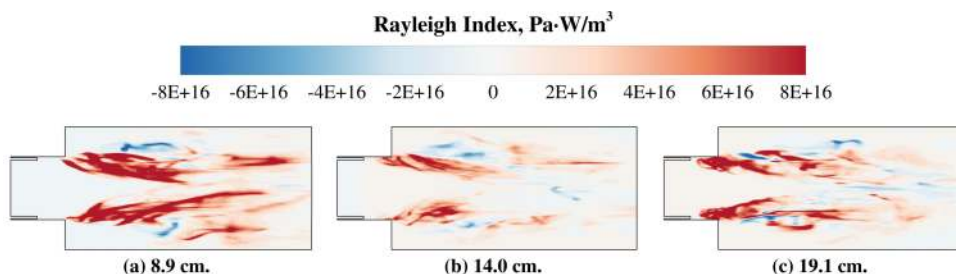


FIG. 14. Rayleigh index. The region shown starts 3 cm upstream of the back step and extends 10 cm downstream of the back step.

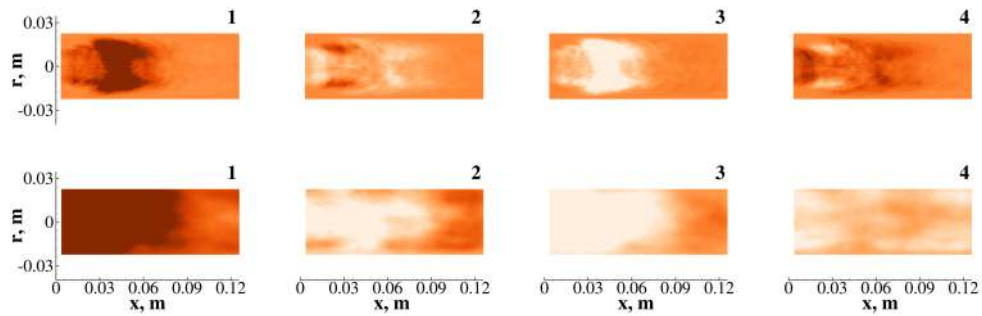


FIG. 15. DMD analysis of the combustion heat release for the simulation (top) and experiment (bottom) for the unstable 14.0 cm length; note that the contour scales in Figures 15 and 16 are different.

Like POD, DMD calculates the eigenmodes from raw data. Unlike POD, which focuses on minimizing the error between the decomposed modes and the original dataset, DMD decomposes the dataset in terms of temporal evolution. The temporal evolution is based on two assumptions: first, evolution between snapshots follows a linear transition map and second, the signal of interest needs to be periodic or quasi-periodic so that one of the snapshots can be represented as a linear combination of the others. With DMD, each eigenmode corresponds to a single frequency, while POD modes are typically associated with multiple frequencies. This capability of DMD to extract modes based on frequency allows the interaction between acoustics and combustion to be viewed as individual modes. Huang *et al.* performed an investigation comparing POD and DMD in the study of acoustically excited combustors; the authors found that DMD was superior to POD.⁶⁷ Motheau *et al.* have also used DMD analysis to identify coherent structures in their instability predictions in gas turbine combustors.²⁵ The coupling and interaction between multiple physical phenomena can be established in terms of the frequency content, and DMD generates a statistically stationary response at specific acoustic modes excluding unwanted frequencies and possible broadband noise from measurements. As a result, DMD results can prove to be a useful tool in experimental and simulation results' comparison.⁶⁸

Here, DMD is used to qualitatively compare the unsteady combustion responses in the experiment and simulations. In the case of the simulation data, the DMD is performed on the combustion heat release. In the experiment, a direct measure of the combustion heat release is not available. Instead, the DMD is performed on CH^* chemiluminescence which has been shown to be correlated to heat release.⁶⁹ CH^* chemiluminescence is the emission of light as a CH^* molecule relaxes from an excited state immediately following a reaction to a lower energy state. In the experiment, the CH^* chemiluminescence image is collected at 10 kHz, which provides only reasonable resolution for the 1L mode containing approximately 10 points per period. To be consistent, heat release from the simulation is down-sampled to a sample rate of 10 kHz, and the domain for analysis is limited to first 12.7 cm downstream of the dump plane which corresponds to the dimension of the quart

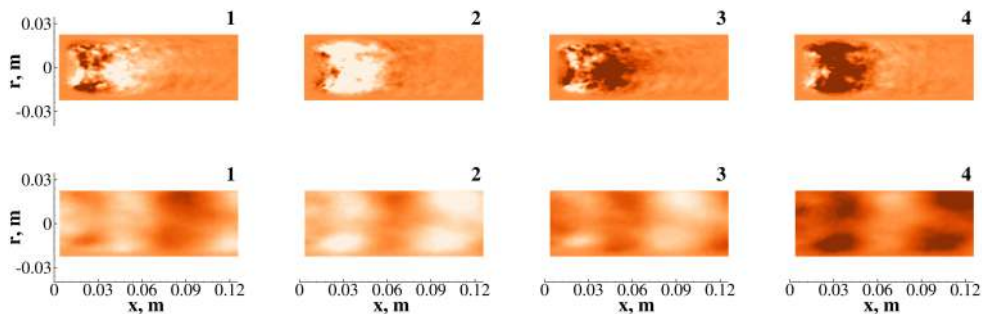


FIG. 16. DMD analysis of the combustion heat release for the simulation (top) and experiment (bottom) for the stable 8.9 cm length; note that the contour scales in Figures 15 and 16 are different.

window in the experiment. Simulation results have been post-processed to yield a line-of-sight measurement which is similar to what is captured by the camera.⁷⁰

Figure 15 shows a DMD analysis of the unsteady heat release for simulation results and experimental data for the unstable 14.0 cm post length case. The four images are taken over the course of a single cycle and contours are intended to show relative magnitudes only. The figure shows a complete cycle starting with high pressure at time 1 and decreases to a minimum pressure at time 3 and increasing again at time 4, before repeating again at time 1. Both the experiment and simulation show the coupling of the heat release and pressure near the back step with the maximum heat release occurring at the peak pressure and less heat release at the cycle trough. A similar cycle is shown for the stable 8.9 cm case in Figure 16, where the overall amplitudes are lower. The simulation shows that there is less pronounced coupling at the back step consistent with the experimental results. The experiment does, however, show activity at the downstream end of the captured region that is not observed in the simulation.

V. SUMMARY AND CONCLUSIONS

Couplings between acoustics, hydrodynamics, and heat release were studied with a simulation of self-excited combustion dynamics in a model rocket combustor. The experiment presented three stability regimes for the simulation: highly unstable, moderately stable, and a bifurcated regime that could be close to one or the other. Based on the predicted and measured pressure fields, the regimes with the more repeatable behavior were matched well by the simulations. Comparisons were based on both instability amplitudes and spatial mode characteristics. The simulation of the bifurcated regime gave amplitudes that were approximately twice that of an unstable experimental realization, with power spectra that matched the experiment.

Results from the simulations were used to characterize and investigate the physical mechanisms and flows associated with each regime. Instability behavior was seen to depend on the complex mode structure near the combustor dump plane where reflected waves from the sonic boundaries at the combustor exit and the oxidizer tube inlet affect the unsteady distribution of fuel near the dump plane. A common feature between instabilities predicted in both the repeatable unstable regime and the bifurcated regime was an interruption in the fuel flow caused by a local high amplitude compression, resulting in a detached flame. When the fuel flow resumes, there is no steady ignition source and the unburnt fuel can premix with the warm oxidizer in the shear layer.

Two types of reignition events were observed that led to high-amplitude instabilities. The reignition was coincident either with the arrival of a downstream-running compression from the post (“post-coupled mode”) or an upstream-running compression in the combustor (“vortex convection mode”). The post-coupled mode was seen when the oxidizer tube length was short, and reignition occurred before the upstream-running wave approached the dump plane. In the post-coupled mode, the compression wave forces itself into the combustor at a relatively low point in the combustor’s pressure cycle causing a large radial pressure gradient. The fuel accumulated in the shear layer is pushed radially outward into the hot gas in the recirculation region, resulting in a massive reignition near the face and a large pressure spike. In the vortex convection mode at the longer tube length, the downstream-running compression wave enters the combustor when the local pressure is considerably higher and there are no large radial pressure gradients to affect the fuel. It remains in the shear layer and re-ignites further downstream coincident with the compression wave reflected from downstream.

Plots of the Rayleigh index indicating the cross-section of pressure and heat release modes were not predictive of the trends observed numerically and experimentally. It was concluded that other driving and damping mechanisms were operating along with the Rayleigh mechanism. DMD analyses carried out for the first longitudinal model frequency indicated reasonable qualitative agreement for the unsteady combustion response, especially at the unstable post length, while at the shorter stable post length, the computational predictions indicate that the combustion response extends further downstream than is evident in the measurements.

The combination of adiabatic wall treatment and a single-step combustion reaction produces high predicted values of temperature and speed of sound, resulting in frequencies and average

chamber pressures that are approximately 15% higher than measured values. It is reasonable to consider this as a possible reason why instability is predicted in the bifurcation regime, at amplitudes that are twice as high what is measured. In the simulation, there is no heat loss near the wall, near-wall gas temperatures are high, the ignition delay time is short, and the flame temperatures are high. In the experiment, however, the wall acts as a heat sink that could possibly extinguish local ignition. The vortex convection mode of instability that is predicted in the bifurcation regime may be particularly susceptible to these modeling approximations, because it depends on compressive heating of a premixed system for ignition, and these nascent ignition events may be quenched by heat loss to the wall in the experiment. Improvements in the thermal treatment of the wall (or conversely an experiment that provides near-adiabatic wall conditions), a chemical kinetics set that more accurately predicts the auto-ignition time, and improved turbulent combustion models are all suggested as topics for future research.

ACKNOWLEDGMENTS

Computing resources were provided by the DoD High Performance Computing Modernization Program. The authors also acknowledge funding from Analytical Mechanics Association, Inc., and NASA under Award No. NNL12AA09C, with Kevin Tucker of Marshall Space Flight Center as Technical Monitor.

- ¹ J. Rayleigh, "The explanation of certain acoustical phenomena," *Nature* **18**, 319-321 (1878).
- ² R. L. Raun, M. W. Beckstead, J. C. Finlinton, and K. P. Brooks, "A review of rijke tubes, rijke burners and related devices," *Prog. Energy Combust. Sci.* **19**(4), 313-364 (1993).
- ³ D. Harje and F. Reardon, "Liquid propellant rocket combustion instability," NASA Technical Report (NASA-SP-194, Washington D.C., 1972).
- ⁴ F. Culick, "Unsteady motions in combustion Chambers for propulsion systems," NATO Research and Technology Organization AGARDograph RTO-AG-AVT-039, 2006.
- ⁵ T. C. Lieuwen and V. Yang, *Combustion Instabilities in Gas Turbine Engines: Operational Experience, Fundamental Mechanisms and Modeling* (AIAA, Reston, VA, 2005).
- ⁶ A. P. Dowling and S. R. Stow, "Acoustic analysis of gas turbine combustors," *J. Propul. Power* **19**(5), 751-764 (2003).
- ⁷ J. E. Crump, K. C. Schadow, V. Yang, and F. E. Culick, "Longitudinal combustion instabilities in ramjet engines identification of acoustic modes," *J. Propul. Power* **2**(2), 105-109 (1986).
- ⁸ U. G. Hegde, D. Reuter, B. R. Daniel, and B. T. Zinn, "Flame driving of longitudinal instabilities in dump type ramjet combustors," *Combust. Sci. Technol.* **55**(4-6), 125-138 (1987).
- ⁹ J. Choi, M. Fuhua, and V. Yang, "Combustion oscillations in a scramjet engine combustor with transverse fuel injection," *Proc. Combust. Inst.* **30**(2), 2851-2858 (2005).
- ¹⁰ E. T. Curran, W. H. Heiser, and D. T. Pratt, "Fluid phenomena in scramjet combustion systems," *Annu. Rev. Fluid Mech.* **28**(1), 323-360 (1996).
- ¹¹ D. Rockwell, "Oscillations of impinging shear layers," *AIAA Journal* **21**(5), 645-664 (1983).
- ¹² C. Ho and S. Nosseir, "Dynamics of an impinging jet. Part 1. The feedback phenomenon," *J. Fluid Mech.* **105**, 119-142 (1981).
- ¹³ T. Schmitt, J. Rodriguez, I. Leyva, and S. Candel, "Experiments and numerical simulations of mixing under supercritical conditions," *Phys. Fluids* **24**, 055104 (2012).
- ¹⁴ D. E. Rogers and F. Marble, "A mechanism for high-frequency oscillation in ramjet combustors and afterburners," *J. Jet Propul.* **26**(6), 456-462 (1956).
- ¹⁵ D. A. Smith and E. E. Zukoski, "Combustion instability sustained by unsteady vortex combustion," in 21st Joint Propulsion Conference, Monterey, CA, AIAA Paper No. 85-1248, 1985.
- ¹⁶ K. H. Yu, A. Trouve, and J. W. Daily, "Low-frequency pressure oscillations in a Mopdel ramjet combustor," *J. Fluid Mech.* **232**, 47-72 (1991).
- ¹⁷ T. J. Poinsot, A. Trouve, D. P. Veynante, S. M. Candel, and E. J. Esposito, "Vortex-drive acoustically coupled combustion instabilities," *J. Fluid Mech.* **177**, 265-292 (1987).
- ¹⁸ K. C. Schadow, E. Gutmark, T. P. Parr, D. M. Parr, K. J. Wilson, and J. H. Crump, "Large-scale coherent structures as drivers of combustion instability," in AIAA 19th Fluid Dynamics, Plasma Dynamics and Lasers Conference, Honolulu, HI, AIAA Paper No. 87-1326, 1987.
- ¹⁹ K. C. Schadow, E. Gutmark, T. P. Parr, D. M. Parr, K. J. Wilson, and J. E. Crump, "Large-scale coherent structures as drivers of combustion instability," *Combust. Sci. Technol.* **64**(4-6), 167-186 (1989).
- ²⁰ F. E. Marble and S. M. Candel, "Acoustic disturbance from Gas non-uniformities convected through a nozzle," *J. Sound Vib.* **55**(2), 225-243 (1977).
- ²¹ C. S. Goh and A. S. Morgans, "The influence of entropy waves on the thermoacoustic stability of a model combustor," *Combust. Sci. Technol.* **185**(2), 249-264 (2013).
- ²² M. Zhu, A. P. Dowling, and K. N. Bray, "Self-excited oscillations in combustors with Spray atomizers," *J. Eng. Gas Turbines Power* **4**, 779-786 (2001).
- ²³ Z. Yao, Y. Gao, M. Zhu, A. P. Dowling, and K. N. Bray, "Combustion rumble prediction with integrated computational-fluid-dynamics/low-order-model methods," *J. Propul. Power* **28**(5), 1015-1025 (2012).

- ²⁴ S. Hochgreb, D. J. Dennis, I. Ayranci, W. Bainbridge, and S. Cant, "Forced and self-excited instabilities from lean premixed, liquid-fuelled aeroengine injectors at high pressures at temperatures," in *ASME Turbo Expo 2013* (ASME, San Antonio, TX, 2013), Paper No. GT2013-9531.
- ²⁵ E. Motheau, F. Nicoud, and T. Poinso, "Mixed acoustic-entropy combustion instabilities in gas turbines," *J. Fluid Mech.* **749**, 542-576 (2014).
- ²⁶ R. Garby, L. Selle, and T. Poinso, "Large-eddy simulation of combustion instabilities in a variable-length combustor," *C. R. Mécanique* **341**(1-2), 220-229 (2013).
- ²⁷ T. Schuller, D. Durox, and S. Candel, "Self-induced combustion oscillations of laminar premixed flames stabilized on annular burners," *Combust. Flame* **135**(4), 525-537 (2003).
- ²⁸ S. Ducruix, T. Schuller, D. Durox, and S. Candel, "Combustion dynamics and instabilities: Elementary coupling and driving mechanisms," *J. Propul. Power* **19**(5), 722-736 (2003).
- ²⁹ L. Crocco and S. Cheng, "Theory of combustion instability in liquid propellant rockets," in *AGARDograph No. 8* (Butterworths Scientific Publications, London, 1956).
- ³⁰ G. Boudier, N. Lamarque, G. Staffelbach, L. Y. Gicquel, and T. Poinso, "Thermo-acoustic stability of a helicopter gas turbine combustor using large eddy simulation," *Int. J. Aeroacoustics* **8**, 69-94 (2009).
- ³¹ G. Staffelbach, L. Y. Gicquel, G. Boudier, and T. Poinso, "Large eddy simulations of self-excited azimuthal modes in annular combustors," *Proc. Combust. Inst.* **32**, 2909-2916 (2009).
- ³² P. Schmitt, T. Poinso, B. Schuermans, and K. P. Geigle, "Large-eddy simulation and experimental study of heat transfer, nitric oxide emissions and combustion instability in a swirled turbulent high-pressure burner," *J. Fluid Mech.* **570**, 17-46 (2007).
- ³³ M. Masquelet and S. Menon, "Large eddy simulation of flame-turbulence interactions in a shear coaxial injector," *J. Propul. Power* **26**, 924-935 (2010).
- ³⁴ M. Suresh and W. Jou, "Large-eddy simulations of combustion instability in an axisymmetric ramjet combustor," *Combust. Sci. Technol.* **75**(1-3), 53-72 (1991).
- ³⁵ S. Srinivasan, R. Ranjan, and S. Menon, "Flame dynamics during combustion instability in a high-pressure, shear-coaxial injector combustor," *Flow, Turbul. Combust.* **94**(1), 237-262 (2015).
- ³⁶ K. Miller, J. Sisco, N. Nugent, and W. Anderson, "Combustion instability with a single-element swirl injector," *J. Propul. Power* **23**(5), 1102-1112 (2007).
- ³⁷ Y. Yu, J. Sisco, S. Rosen, A. Madhav, and W. Anderson, "Spontaneous longitudinal combustion instability in a continuously-variable resonance combustor," *J. Propul. Power* **28**(5), 876-887 (2012).
- ³⁸ Y. Yu, "Experimental and analytical investigations of longitudinal combustion instability in a continuously variable resonance combustor (CVRC)," Ph.D. thesis (Purdue University, West Lafayette, IN, 2009).
- ³⁹ T. Feldman, "Unstable combustion processes for a single element shear/coax injector in a longitudinal combustor," M.S. thesis (Purdue University, West Lafayette, IN, 2013).
- ⁴⁰ R. Smith, G. Xia, W. Anderson, and C. L. Merkle, "Computational simulations of the effect of back step height on non-premixed combustion instability," *AIAA J.* **48**(9), 1857-1868 (2010).
- ⁴¹ R. Smith, "Computational investigations of high frequency acoustics and instabilities in a single-element rocket combustor," Ph.D. thesis (Purdue University, West Lafayette, IN, 2010).
- ⁴² R. Smith, G. Xia, W. Anderson, and C. Merkle, "Computational studies of the effects of oxidizer injector length on combustion instability," *Combust. Theory Model.* **12**, 341-368 (2012).
- ⁴³ M. Harvazinski, "Modeling self-excited combustion instabilities using a combination of two- and three-dimensional simulations," Ph.D. thesis (Purdue University, West Lafayette, IN, 2012).
- ⁴⁴ M. Harvazinski, W. Anderson, and C. Merkle, "Analysis of self-excited combustion instability using two- and three-dimensional simulations," *J. Propul. Power* **29**(2), 396-409 (2013).
- ⁴⁵ T. Feldman, M. Harvazinski, C. Merkle, and W. Anderson, "Comparison between simulation and measurement of self-excited combustion instability," in 48th AIAA/ASME/SAE/ASEE Joint Propulsion Conference and Exhibit, Atlanta, GA, AIAA Paper No. 2012-4088, 2012.
- ⁴⁶ R. Garby, L. Selle, and T. Poinso, "Analysis of the impact of heat losses on an unstable model rocket-engine combustor using large-eddy simulation," in 48th AIAA/ASME/SAE/ASEE Joint Propulsion Conference and Exhibit, Atlanta, GA, AIAA Paper No. 2012-4085, 2012.
- ⁴⁷ W. Marshall, S. Pal, R. Woodward, and R. Santoro, "Benchmark Wall heat flux data for GO2/GH2 single element combustor," AIAA Paper No. 2005-3572, 2005.
- ⁴⁸ C. Lian, G. Xia, and C. Merkle, "Solution-limited time stepping to enhance reliability in CFD applications," *J. Comput. Phys.* **228**, 4836-4857 (2009).
- ⁴⁹ D. Li, G. Xia, V. Sankaran, and C. Merkle, "Computational framework for complex fluids applications," in *Computational Fluid Dynamics 2004* (Springer, Berlin, Heidelberg, 2006), pp. 619-624.
- ⁵⁰ G. Xia, V. Sankaran, D. Li, and C. Merkle, "Modeling of turbulent mixing layer dynamics in ultra-high pressure flows," in 36th AIAA Fluid Dynamics Conference and Exhibit, San Francisco, CA, AIAA Paper No. 2006-3729, 2006.
- ⁵¹ C. Lian, G. Xia, and C. Merkle, "Impact of source terms on reliability of CFD algorithms," *Comput. Fluids* **39**, 1909-1922 (2010).
- ⁵² P. Spalart, "Detached eddy simulations," *Ann. Rev. Fluid Mech.* **41**, 181-202 (2009).
- ⁵³ A. Travin, M. Shur, and P. Spalart, "Physical and numerical upgrades in the detached-eddy simulation of complex turbulent flows," *Fluid Mech. Its Appl.* **65**, 239-254 (2002).
- ⁵⁴ D. Wilcox, *Turbulence Modeling for CFD*, 2nd ed. (DCW Industries, La Cañada, 1998).
- ⁵⁵ D. Wilcox, "Formulation of the k- ω turbulence model revisited," *AIAA J.* **46**(11), 2823-2838 (2008).
- ⁵⁶ C. Westbrook and F. Dryer, "Simplified reaction mechanisms for the oxidation of hydrocarbon fuels in flames," *Combust. Sci. Technol.* **27**, 31-43 (1981).
- ⁵⁷ O. Colin, F. Ducros, D. Veynante, and T. Poinso, "A thickened flame model for large eddy simulations of turbulent premixed combustion," *Phys. Fluids* **12**(7), 1843-1863 (2000).

- ⁵⁸ P. Tucker, S. Menon, C. Merkle, J. Oefelein, and V. Yang, "Validation of high-fidelity CFD simulations for rocket injector design," in AIAA/ASME/ASEE Joint Propulsion Conference and Exhibit, Hartford, CT, AIAA Paper No. 2008-5226, 2008.
- ⁵⁹ C. Lian and C. Merkle, "Effects of chamber diameter on the flowfield in uni-element rocket combustors," *J. Propul. Power* **28**(3), 568-584 (2012).
- ⁶⁰ C. Pozrikidis, *Fluid Dynamics: Theory, Computation, and Numerical Simulation*, 2nd ed. (Springer, 2009), pp. 343-350.
- ⁶¹ A. Ghosh and K. Yu, "Effect of density gradient on flame-acoustic interaction," *J. Propul. Power* **30**(3), 717-726 (2014).
- ⁶² N. Peters, *Turbulent Combustion* (Cambridge University Press, New York, 2000).
- ⁶³ K. Kuo, *Principles of Combustion*, 2nd ed. (Wiley, 2005).
- ⁶⁴ F. Nicoud and T. Poinso, "Thermoacoustic instabilities: Should the Rayleigh criterion be extended to include entropy changes?," *Combust. Flame* **142**, 153-159 (2005).
- ⁶⁵ P. Schmid, "Dynamic mode decomposition of numerical and experimental data," *J. Fluid Mech.* **656**, 5-28 (2010).
- ⁶⁶ G. Berkooz, P. Holmes, and J. L. Lumeley, "The proper orthogonal decomposition in the analysis of turbulent flows," *Annu. Rev. Fluid Mech.* **25**, 539-575 (1993).
- ⁶⁷ C. Huang, M. Harvazinski, W. Anderson, and V. Sankaran, "Analysis of self-excited combustion instability using decomposition techniques," in 51st AIAA ASM Including the New Horizons Forum and Aerospace Exposition, Grapevine, TX, AIAA Paper No. 2013-1007, 2013.
- ⁶⁸ J. S. Hardi, W. Z. Hallum, C. Huang, and W. E. Anderson, "Development of validation approaches for numerical simulations of combustion instability using flame imaging," in 50th AIAA/ASME/SAE/ASEE Joint Propulsion Conference, Cleveland, OH, AIAA Paper No. 2014-3775, 2014.
- ⁶⁹ V. Nori and J. Seitzman, "Chemiluminescence modeling for combustion diagnostics," *Proc. Combust. Inst.* **32**, 895-903 (2009).
- ⁷⁰ H. Ruder, T. Ertl, F. Geyer, H. Herold, and U. Kraus, "Line-of-sight integration: A powerful tool for visualization of three-dimensional scalar fields," *Comput. Graphics* **13**(2), 223-228 (1989).